



Universiteit Utrecht



Thesis Project

Methane release from meteoritic material under Mars – like UV radiation



Master student
Kyriacos Chrysostomou (3922391)

Supervisor / first reviewer
Prof. Dr. Thomas Röckmann, Utrecht University

Second reviewer
Dr. Ir. Inge Loes ten Kate, Utrecht University

Institute for Marine and Atmospheric research Utrecht (IMAU), The Netherlands

August 2014

Acknowledgment

I want to dedicate this thesis project to my parents to express my gratitude for their moral and financial support throughout the two years of my master program. Many thanks also to my grandmother and godmother for their significant contribution in completing my studies. I am sincerely grateful to my supervisor Prof. Dr. Thomas Röckmann for giving me the opportunity to work on such an interesting topic and use his laboratory facilities. His guidance, support, constructive criticism and advices were fundamental in the understanding and completion of all the tasks of the project.

Special thanks also to Michiel Kienhuis, Paul Mason, Inge Loes ten Kate and Lubos Polerecky from the department of Geosciences for their great help and support. Furthermore, I would also like to thank the technicians Carina van der Veen and Henk Snellen for their help in building the experimental setup, Uli Ott and Frank Keppler for providing the meteoritic material, Huib van Weelden for the calibration of the lamps, Otto Stiekema for preparation and polishing of the targets and Marion Fruechtl for all the help she provided me with. Many thanks to my friends Teresa Macarico Morins and Anthi Chrysanthou for helping and supporting me at every step of my master course.

Table of Contents

1 Abstract	5
2 Introduction	6
2.1 Martian methane	6
2.2 Micrometeorite rain.....	7
2.3 Martian UV radiation flux	8
2.4 Meteorites	8
2.4.1 Origin.....	8
2.4.2 Chondrites.....	9
2.4.3 Origin of organics	10
2.4.4 Carbonaceous chondrites of CM group	11
2.4.4.1 Murchison meteorite – CM2.....	11
2.4.4.2 CM features	12
2.4.4.3 Location of organic molecules	12
2.4.4.4 OM solubility.....	13
2.4.4.5 Insoluble organic fraction (IOM – 70% of total C)	13
2.4.4.6 Soluble organic fraction (SOM – 30% of total C)	14
2.4.5 Meteoritic organic matter interactions with ultraviolet radiation.....	15
2.4.5.1 Release of hydrocarbons	15
2.4.5.2 Mineral composition	16
2.4.5.3 Temperature dependence	16
2.4.5.4 Pressure dependence	17
2.4.5.5 Wavelength dependence	17
2.4.5.6. Methane production on Mars	17
2.5 Objectives.....	18
3 Methodology	19
3.1 Experimental description	19
3.2 Irradiation experiments setup	20

3.2.1 Irradiation reactor features	21
3.2.2 Xenon arc lamp	22
3.2.2.1 Light generation mechanism	22
3.2.2.2 Spectral calibration, effect of 45°mirror and Suprasil disk.....	23
3.2.2.3 Waldmann UV meter	25
3.2.3 Picarro Fast CO ₂ /CH ₄ /H ₂ O analyzer	26
3.2.3.1 Cavity ring-down spectroscopy.....	26
3.2.3.2 Calculations.....	27
3.2.4 Methane emission experiments	29
3.2.5 Blank measurements	30
3.2.6 Gas stability measurements.....	30
3.2.7 Meteorite samples.....	30
3.3 UV penetration experiments	32
3.3.1 Targets (preparation and irradiation).....	32
3.3.2 Scanning electron microscopy (SEM)	34
3.3.3 NanoSIMS.....	35
3.3.4 Calculating the emission rates	36
3.3.5 Calculating the penetration depth from the emission rate values	38
4 Results.....	39
4.1 Instrument stability.....	39
4.2 Blank measurements	41
4.5 UV intensity of experiments	45
4.6 Methane emission experiments 1 – 4	46
4.6.1 Methane mixing ratios.....	46
4.6.2 Emission rates	49
4.6.3 Methane mass production.....	53
4.6.3 Penetration depth estimation (from methane gas values)	57
4.7 Irradiated target experiments	59
5 Conclusions – Discussion.....	72
5.1 Methane byproduct	72

5.2 Emission rates of methane	72
5.3 Methane emission in carbon limited / photon limited conditions.....	73
5.4 Penetration depth from methane mass values	74
5.5 Lack of carbon grains	74
5.6 Carbon depletion	74
5.7 Penetration depth of UV radiation	76
6 Appendix.....	77
6.1 Carboxylic acids.....	77
6.2 Amino acids.....	77
6.3 Hydrocarbons.....	79
6.5 Experimental pictures	79
7 References	82

1 Abstract

Since the detection of Martian atmospheric methane in 2004, a lot of scientific debate has followed concerning the potential sources and mechanisms that cause its presence. The short photolytic lifetime of methane on Mars (Krasnopolsky et al., 2004) implies the existence of a constant emission source over or below the surface of the planet. Recommended geological and biological emission processes are confoundedly small and unable to explain the observed mixing ratio values.

Mars' location next to the asteroid belt exposes the planet to a heavy rain of meteorites; with some types like carbonaceous chondrites containing a few percent of organic material. Unlike Earth, the atmosphere of Mars does not have an ozone layer that filters a significant fraction of ultraviolet (UV) radiation. In this project it is shown that when a carbonaceous chondrite type (Murchison meteorite) is exposed to Mars surface like UV radiation levels, a part of its organic molecules interacting with UV is converted and outgassed as methane. By looking at the depth profiles of different elements through nanoSIMS analysis, an effort was made to investigate the solid carbon balance and distinguish the penetration depth of UV under the meteoritic surface.

The understanding of meteorite interactions with ultraviolet radiation can give a more thorough view of their contribution to the atmospheric composition of Mars, as well as to the primordial Earth.

2 Introduction

2.1 Martian methane

In 2004 methane was detected for the first time in the atmosphere of Mars through an Earth based telescopic spectrometer in Hawaii (Krasnopolsky et al., 2004). Since then different scientific reports range global average methane mixing ratios between 8 – 15 parts per billion by volume (ppbv), with latitudinal, seasonal and interannual variabilities (Formisano et al., 2004; Krasnopolsky, 2012; Mumma et al., 2009). A recent reanalysis of the data have proposed an average upper boundary of 3 ppbv (Krasnopolsky, 2012; Webster et al., 2013).

The photochemical lifetime of methane on Mars is restricted between 250 and 670 terrestrial years (Wong, 2003). By now, the only accepted process responsible for the atmospheric destruction of methane is the Lyman- α photochemical reaction that occurs in the upper Martian atmosphere (Lefevre and Forget, 2009). By accepting this process as the only methane sink, the observed mole fractions of methane need a carbon flux of 200 - 300 t yr⁻¹ to be achieved (Atreya et al., 2007). As long as the detection of Martian methane is correct, the existence of constant methane sources over or below the surface of the planet was proposed that would produce these annual fluxes.

The great interest in Martian methane is due to the fact that the terrestrial counterpart is mostly produced biologically. A lot of discussion has been ongoing concerning the possible origins and mechanisms that cause methane to be present in Martian air. Among the suggested processes are geothermal release, outgassing from impacts of extraterrestrial bodies (comets and asteroids), serpentinization of minerals and biological pathways (Etiope et al., 2011; Schuerger et al., 2011; Shkrob et al., 2010). Nonetheless, the potential methane contribution from all the recommended sources is relatively trivial and unable to explain the observed mixing ratio values (Schuerger et al., 2011). Recently the outgassing of methane from various Mars-like

UV-irradiated organics has been proven (Schuerger et al., 2011), which led to the suggestion that micrometeorite input could be the continuous methane source scientists were searching for (Keppler et al., 2012).

2.2 Micrometeorite rain

Mars orbits next to a vast region of rock bodies known as the asteroid belt. The distance between the planet and the asteroid belt (72×10^6 km) is approximately 10% shorter than the space between Earth and Mars (78×10^6 km), exposing the red planet to a heavy input of extra-planetary material (Flynn, 1996). Relatively minimal amounts of methane are released (due to pyrolysis and ablation processes) from the surface of these solid rocks as they enter the atmosphere of the planet. The material ending up on the surface of Mars has a mass flow of 2700 to 59000 t yr⁻¹, is principally μm scaled (micrometeorites) and remains mostly unmelted (Flynn, 1996, 1990).

In 1976, two space missions landed on the surface of Mars to detect and study the organics of Mars, but no evidence was found. Recent reanalysis of soil samples collected by Viking 1 and 2 hinted towards tiny concentrations of organic material (Navarro-González et al., 2010). Environmental factors are believed to be the reason behind the lack of organics paradox, for example UV radiation, oxidation reactions can cause the fast destruction of organic molecules from the Martian soil. Solar UV can react with organics in the top millimeter layers of the Martian surface, energetic particles/cosmic rays can penetrate and react with organics down to a few meters, while oxidation processes could be active down to a depth of 200 meters (Poch et al., 2013). Keppler et al. 2012 showed that ultraviolet radiation interactions with micrometeorites (with chemical composition similar to carbonaceous chondrites and carbon content around 2%) could reproduce the suggested methane mixing ratio values for the atmosphere of Mars and could partly explain the organic paradox for the surface of the planet.

2.3 Martian UV radiation flux

By now, none of the Martian space landers has taken in situ measurements of the radiative spectrum of the sun that eventually reaches the surface of Marsⁱ. The REMS package on Curiosity rover does measure UV intensity, but no papers were published yet. All the available surface radiation data are based on theoretical models that calculate the intensity of each wavelength reaching the top of the atmosphere (from remote observations) and their flux towards the Martian surface. Concerning UV radiation, models take into account that every wavelength smaller than 190 nm is absorbed by atmospheric CO₂ (mole fraction = 95.97%). The transmittance of the remaining ultraviolet spectrum is controlled by the local aerosol loading and ozone concentration (Poch et al., 2013). Unlike Earth, the atmosphere of Mars does not have an ozone layer of global extension that blocks a significant fraction of UV radiation, so UV wavelengths longer than 190 nm reach the surface of the red planet (while on earth any wavelength shorter than 350 nm is blocked). Considerable O₃ mixing ratios can only be found during winter periods at high latitudes (Patel et al., 2002).

2.4 Meteorites

2.4.1 Origin

Meteorites refer to extraterrestrial debris materials mostly originating from fragments of asteroids or comets (referred to as parent bodies) that penetrate the atmosphere and succeed in reaching a planetary surface. It is most likely that their matrix is a result of condensation and evaporation processes under the high temperatures occurring in the solar nebulaⁱⁱ. According to their composition and texture they are classified into two categories, chondrites and achondrites. The aim of this categorization is to reveal meteorites with similar genetic processes or origins,

ⁱ One of the tasks of Beagle 2 mission was to land on Mars in 2003 and measure the UV spectrum (190 - 400nm). The mission failed just before landing time when contact with the spacecraft was lost.

ⁱⁱ The rotating flattened cloud of gases and dust from which a star and its rest of the bodies in the solar system will finally take shape.

and to uncover potential links among different groups. The chemical composition of each group of meteorites differs with respect to volatile elements, metallic oxygen, magnesium silicates, and organic material consistency (Scott and Krot, 2014).

After their formation, the majority of chondrites were subjected to either aqueous or thermal modifications on their parent asteroids or shock metamorphism during impact events. These forceful processes altered the birth characteristics of the plurality of meteorites, so their formation conditions were completely erased. In a few cases the complete melting of meteorites was prevented, and thus the physicochemical characteristics corresponding to their genetic characteristics were largely maintained. Such materials can be considered as historical artifacts, which can provide data about the chemical presence of elements even before the complete formation of our solar system (Krot et al., 2007).

2.4.2 Chondrites

Chondrites are separated into carbonaceous (carbon enriched), ordinary and enstatite classes. Based on their chemistry and oxygen isotopes, mineralogy and petrography the class of carbonaceous chondrite is further split into 8 groupsⁱⁱⁱ: CL, CM, CR, CH, CB, CV, CK and CO. The group name of a meteorite is followed by a number from 1 to 6, which specifies the degree at which aqueous alteration and thermal metamorphism was momentous in altering the chemistry of the parent asteroid (*Figure 1*) (Krot et al., 2007).

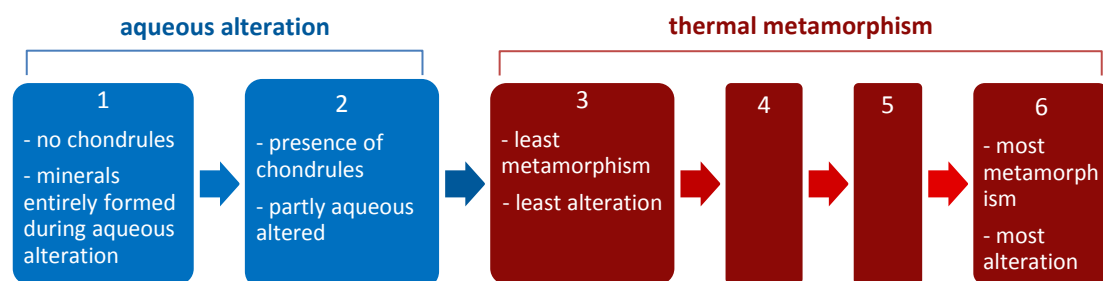


Figure 1: Degree of aqueous and thermal alteration of meteorites

ⁱⁱⁱ There are also many meteorites that don't fall in these groups and they are characterized as ungrouped

2.4.3 Origin of organics

Two feasible sources of organic matter (OM) in meteorites have been suggested. It could have been synthesized before the accretion of the parent body or in situ on or in the formed asteroid. Experiments have shown that organic molecules can be present in several astrophysical locations including protosolar/protostellar disks, which could potentially be enclosed in any formed asteroid (Gilmour, 2003; Scott and Krot, 2014). The Miller – Urey experiment in the 50s revealed that organic material can be composed from simple inorganic molecules under specific environmental conditions (Miller and Urey, 1959). Such conditions could occur on the surface of asteroids that would lead to organic molecule formation on the parent body. The presence of specific clay minerals is credited for catalyzing such reactions (Le Guillou et al., 2014). Water is also encapsulated in meteorites as hydroxyl groups attached to minerals, such as phyllosilicates and oxides. Interactions between water particles and OM could have produced new organic molecules like carboxylic acids (Le Guillou et al., 2014).

Isotopic measurements can be used to show whether the genesis of OM was a result of protostellar disk or in situ reactions (Alexander et al., 2010). The study of the CH₄ emissions of UV-irradiated Murchison meteorite (a type of carbonaceous chondrite) that were a product of the photodegradation of its organics, revealed high deuterium bulk δD values that vary between 1070‰ and -90‰ (Figure 2). Such values are not found on Earth, proving the extraterrestrial origin of its OM (Keppler et al., 2012).

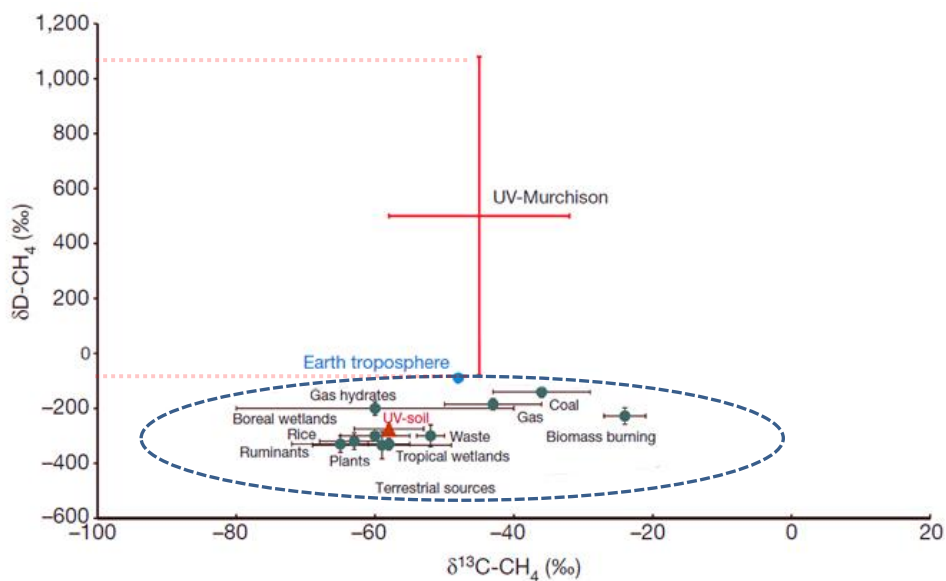


Figure 2: Stable heavy carbon and hydrogen isotope values of methane outgassing from UV irradiated Murchison meteorite samples in relation with the methane sources on Earth (Keppler et al., 2012).

2.4.4 Carbonaceous chondrites of CM group

The group of carbonaceous chondrite meteorites referred to as CM chondrites was named after the Murchison meteorite.

2.4.4.1 Murchison meteorite – CM2

Murchison meteorite is a typical example of a carbonaceous chondrite. Its fall was observed in 1969 near the city of Murchison in Victoria, Australia. One hundred kilograms of this material was almost directly collected, which minimized the effect of terrestrial contamination. The surrounding, outer layer of these fragments was characterized by molten material, yet the interior remained unmodified. Research has revealed that it belongs to the CM2 group of chondritic meteorites. It is the most studied meteorite to present, with respect to its organic material (Airieau et al., 2005).

2.4.4.2 CM features

The oldest dated organic molecules detected on Earth derived from falling carbonaceous chondrite materials. They contain small amounts of carbon ($\approx 1.5 - 4\%$), which are mostly present as organic material. The extensive aqueous modification observed in CM chondrites created high abundance of phyllosilicates^{iv} enriched in heavy stable oxygen isotopes. CM matrix has a relatively high abundance of chondrules, which are small formations principally consisting of olivine and pyroxene (anhydrous silicates) which formed by swift crystallization. Their shape reveals the degree at which they might have melted in their geological history; round shapes denote complete melting and irregular shapes imply partial melt. CM chondrites are consisted also by carbonates, tochilinite, sulfides and magnetite (iron oxides) (Pizzarello and Shock, 2010).

2.4.4.3 Location of organic molecules

Organic matter (OM) can be found in Murchison either as individual grains or diffused. Organic grains are considered the main carbon reservoir of the meteorite and can have a nanoglobule or vague shape (Pizzarello and Shock, 2010). They have shown a high spatial (micron scale) and isotopic heterogeneity, which is likely owed to the miscellany of organic matter during accretion or to different in situ processes (different degree of aqueous reactions) (Le Guillou et al., 2014). Diffused OM is extended throughout the matrix and its presence is correlated with the distribution of Mg-rich phyllosilicates, whose mineral chemistry is between serpentine and saponite. Such minerals have OH groups attached to their molecules, which shows the important role of water in the production and evolution of organic particles. Some surface cracks have been found to be loaded with organic material, indicating the redistribution of OM during aqueous alteration events. The high presence of Na and Cl elements (which are soluble) indicates the high level of aqueous interactions and

^{iv} Sheets of Si_2O_5

leads to the assumption that the fluid was a brine (Le Guillou et al., 2014). Organic molecules were also detected at the interior of phyllosilicates (Le Guillou et al., 2014).

2.4.4.4 OM solubility

Organic material is divided into an insoluble fraction and a fraction that is soluble in water and/or other organic solvents. In individual grains the insoluble organic matter (IOM) counterparts 70% of the total carbon presence and the remaining 30% stands for the soluble organic material (SOM). On the other hand diffused OM mostly consists of soluble molecules (Le Guillou et al., 2014). Warming events and partial melting of ice over the asteroids have led to the formation of the soluble parts found in meteorites (Pizzarello and Shock, 2010). Concerning isotope fractionation^v, many compounds were found to be enriched in D (²H, deuterium), ¹³C and ¹⁵N which denote a genetic environment of very low temperatures (Pizzarello and Shock, 2010).

2.4.4.5 Insoluble organic fraction (IOM – 70% of total C)

The insoluble part of Murchison meteorite is characterized by high heterogeneity with a majority of macromolecular substances, whose average elemental composition is C₁₀₀H₄₆N₁₀O₁₅S_{4.5} (Pizzarello and Shock, 2010). Spectroscopy and decomposition methods (pyrolysis^{vi} or oxidation to its fragments) revealed non – solvable molecules like aromatic rings and branched aliphatic chains. Transmission electron microscopy showed that only 10% of the IOM had specific formations (nanostructures, tubes, spheres etc.), while the remaining fraction was shapeless. Possible “exotic” carbon was also located, which is believed it was created before the birth of the solar system (Le Guillou et al., 2014; Pizzarello and Shock, 2010).

^v Isotopic fractionation reveals molecules synthetic past, since mass differences of the isotopes (different bond formation energy) can lead to conclusions about the physical and chemical environment where these reactions took place.

^{vi} Decomposition provoked by high temperatures

The emission of volatile gases to the surroundings was proven when meteoritic organic material is exposed to extreme conditions such as a hydrothermal vent environments (high temperature and pressure, long presence in water) (Pizzarello and Shock, 2010) or high frequency radiation (UV, cosmic rays) (Poch et al., 2013). This property of meteorite organics reveals the possible contribution of meteorite rain to the organic pool of the primordial Earth.

2.4.4.6 Soluble organic fraction (SOM – 30% of total C)

The high abundance and diversity of SOM in the Murchison meteorite is represented by over a thousand different soluble molecules; from amino acids and polyols to long chained hydrocarbons (up to 30 C atoms)(Pizzarello and Shock, 2010). Nevertheless, it mostly consists of soluble carboxylic acids, which are principally a result of aqueous reactions. Liquid water alteration events can cause the molecular evolution (oxidation, hydrolysis) of aliphatic chains (IOM) into carboxylic acids (SOM) (Le Guillou et al., 2014).

Table 1 shows the abundance of organic compounds found in Murchison meteorite.

Table 1: Concentration of organic compounds found in Murchison meteorite (Gilmour, 2003).

Compounds Abundance	Abundance (ppm)
Carboxylic acids	372.2
Monocarboxylic	332
Dicarboxylic	25.7
α -Hydroxycarboxylic	14.6
Carbon dioxide	106
Sulfonic acids	67
Amino acids	60
Sugars and related compounds	≈60
Dicarboximides .	>50

Hydrocarbons	17 - 64
Aliphatic	12 – 35
Aromatic	15 – 29
Ammonia	19
Ketones	16
Alcohols	11
Aldehydes	11
Amines	8
Pyridinecarboxylic acids	>7
Phosphonic acids	1.5
Purines	1.2
Methane	0.14
Basic N-heterocycles	0.05–0.5
Benzothiophenes	0.3
Carbon monoxide	0.06
Pyrimidines	0.06

2.4.5 Meteoritic organic matter interactions with ultraviolet radiation

Organic material reacts photochemically with UV photons, inducing the outgassing of organic volatiles. The release of such gasses depends on temperature, pressure and wavelength, as well as on the mineral environment that surrounds the organic molecules.

2.4.5.1 Release of hydrocarbons

Chemical reactions induced by interactions of organic molecules with ultraviolet photons primarily cause the production and outgassing of methane. Schuerger et al. 2012 have shown the emission of CH₄ from 15 different UV-irradiated organic substances, while inorganic compounds did not give any methane signal. Gas chromatography has revealed the evolution of other volatile hydrocarbons like

ethane, ethene, propane, propene and butane. Their abundance was lower than methane by two orders of magnitude (Keppler et al., 2012).

2.4.5.2 Mineral composition

The presence of specific minerals adjacent to organics is believed to ease their reactivity with UV light. The presence of iron (III) oxides and silicates catalyzes the production of methane (Bartoszek et al., 2011; Keppler et al., 2012). For example, carboxylic acids undergo photo-Kolbe reactions on the surface of such catalysts that provoke decarboxylation of the molecule and release of methane or other hydrocarbons (Shkrob et al., 2010). Other surface reactions cause the production of free radicals which will eventually react with organics and provoke the emission of volatiles. On the other hand, other minerals like magnesium silicates are weak absorbers of UV, which would allow photons to reach much deeper and react with organics from depths down to a few hundred of micrometers (Bartoszek et al., 2011).

2.4.5.3 Temperature dependence

Temperatures on Mars show a great variability from -143°C at the higher latitudes up to +17°C at the equator. Keppler et al. 2012 studied the temperature dependence of methane production originating from UV-irradiated Murchison meteorite samples, between -190°C to +20°C at 1 atmosphere (1000 mbar). No methane release was recorded below -40°C. Above -20°C, a positive correlation was found for which the emission rate of methane augmented by 18 ng CH₄ g⁻¹ h⁻¹ per 1°C. Schuerger et al. 2011 determined this positive relation between temperatures of -80°C to 20°C. After cooling and re-irradiating the samples, strong methane release was observed even for temperatures down to -30°C (Keppler et al., 2012).

2.4.5.4 Pressure dependence

The atmosphere of Mars is approximately a hundred times thinner than Earth's, characterizing the surface pressure of the planet at 7 mbar. By dropping the pressure conditions down to 5 – 10 mbar, methane emissions from UV-irradiated Murchison samples increased by 2 – 3 times and were recorded even down to temperatures of -80°C (in comparison with 1000 mbar experiments) (Keppler et al., 2012).

2.4.5.5 Wavelength dependence

Irradiation experiments of dry plant biomass as well as Murchison meteorite samples have both shown a UV wavelength dependence of the emission rates of methane. UVB photons (280 – 314 nm) were proven to be the most significant in reacting with organics and producing CH₄, while the remaining wavelengths had only a small effect on emission rates. More specifically, wavelengths from 295 nm to 305 nm determine the efficiency with which radiation causes methane emission (Keppler et al., 2012; Vigano et al., 2008).

2.4.5.6. Methane production on Mars

To characterize the Martian surface environment with respect to its efficiency to convert carbon into methane, Schuerger et al. 2012 calculated the maximum carbon mass that could be converted to methane in a year for the whole surface of the planet. They found that the capability of Martian UV to degrade organics (even at the poles) is three orders of magnitude larger than the quantity that reaches the surface of the planet in a year, characterizing Martian methane production as *carbon-limited*. This means that there is sufficient radiation at each latitude of Mars to react with organic matter and that the production of methane is determined only by the availability of carbon.

2.5 Objectives

The purpose of this 9 month thesis project was to investigate the gas and solid phase of carbon after the UV irradiation of Murchison meteorite samples. Initially, the effort was focused on quantifying and comparing the long term emission rates of methane under Mars – like UV exposure and under higher intensity radiation. Subsequently, the carbon balance of the meteorite was investigated in an effort to discover how deep UV photons manage to penetrate under the surface and react with organic molecules.

In chapter 3, a detailed description of all the used methods, equipment and calculations is given covering both experimental parts of the project. The irradiation setup is explained, as well as the working principle of the Xenon lamp, ring-down spectroscopy, Scanning Electron Microscopy (SEM) and nanoSIMS.

In chapter 4, all the results from the data analysis are analyzed and plotted.

In chapter 5, the conclusions of this project are discussed; some improvements and future experiments are suggested.

In chapter 6, some extra information about the main categories of organic compounds found in Murchison meteorite are given in an Appendix, as well as pictures of the experimental setup.

3 Methodology

For the purpose of this thesis project, 1 gram of a solid fragment and 1 gram of grounded material of the Murchison meteorite was received from MPI in Mainz, Germany. The meteorite was left sealed in its plastic case and it was only opened during sampling, to minimize dust and bacterial exposure from the surrounding air. Terrestrial contamination, as well as external organic sources from the plastic container and the handling (gloves, clamp etc.) of the meteorite material is possible. Since Murchison meteorite contains 2% of organics and the previously mentioned contamination sources are on the order of parts per million (Schuerger et al., 2012), external carbon can be considered as a minor factor.

3.1 Experimental description

The experimental part of the project was divided into two sections. During the first section, the gas phase conversion of meteoritic carbon into methane was studied at the *Institute of Marine and Atmospheric research Utrecht (IMAU)*. It included the construction of a setup with which a series of irradiation experiments of meteoritic samples would be undertaken to measure the emission rates of outgassing methane.

The purpose of the second section of the project was to investigate the solid carbon balance after interaction of UV radiation with meteorite material. To accomplish that, irradiated samples were transferred to the *Institute of Earth Sciences Utrecht (IVAU)* where they were subjected to Scanning Electron Microscopy (SEM) and nanoSIMS analysis. SEM application revealed the topography and elemental distribution of each sample, according to which the most interesting locations were specified to further apply the nanoSIMS.

3.2 Irradiation experiments setup

The experimental setup is shown in *Figure 3*, *Figure 37* and *Figure 38*. It was designed to be leak tight so that no interactions with the external environment would occur. The reactor, within which the meteorite samples were placed, was connected to a gas cylinder containing compressed, normal air. Two mass flow controllers were placed after the gas cylinder to flush air through the system with a stable flow rate and to prevent any undesirable overpressure conditions. The normal air gas was passing from the gas cylinder to the reactor and was eventually flushed towards a Cavity ring – down spectrometer (CRDS) which was set to measure methane mixing ratios every second with a precision of ± 1 ppbv. Two established valves allowed the system to measure methane levels of gas that derived either from the reactor (position 1) or directly from the gas cylinder (position 2), as it is shown in *Figure 3*. The switching of the valves from position 1 to position 2 and vice versa was regulated from automatically from the computer.

A Xenon lamp (Osram) was used as the light source to irradiate the content of the reactor. Its beam was reflected through an attached 45° mirror over the reactor. UV photons passed through the quartz plate (its UV transparency is explained in section 3.2.2.2) that was used to seal the top of the reactor, and reached the meteorite sample. UV intensity values of each experiment were measured by a UV meter. The reactor, along with the Xenon lamp, was placed in a bigger sized chamber to provide protection of the laboratory environment from UV radiation and to avoid contact with ozone for the researchers. For this reason the chamber was attached to the lab ventilation through which removed all gases, including O_3 .

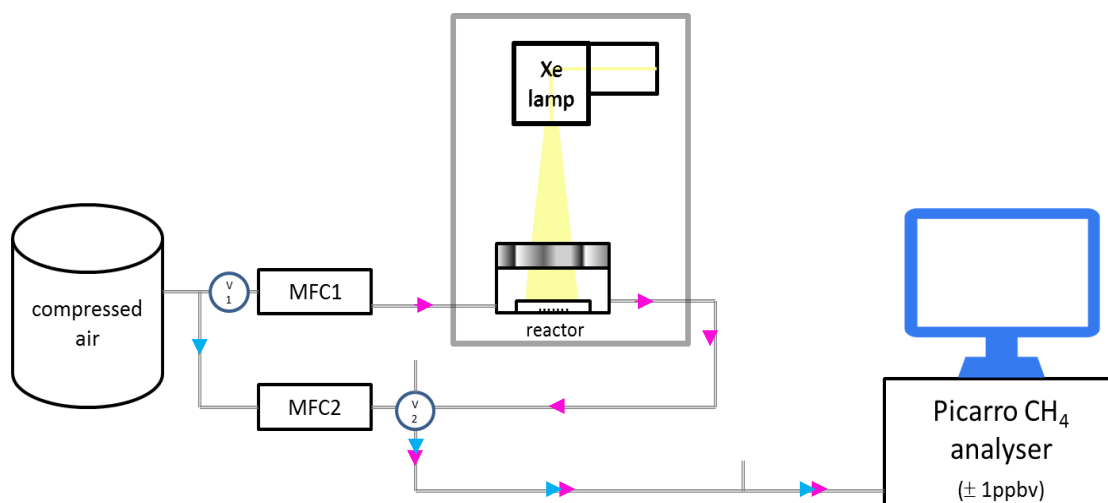


Figure 3: Setup illustration of irradiation experiments. Pink arrows show the route of the flushed air gas during position 1 from the gas cylinder (through the chamber) towards the methane analyzer, while blue arrows denote its direction during position 2 (directly to the CRDS). MFC1 and MFC2 represent the two mass flow controllers that were flushing normal air through the system at 70 and 50 ml min⁻¹, respectively. Valve 1 and 2 (V1 and V2) were responsible for the automatic switching between the two steps, by allowing/blocking the flow beyond them. The Xenon lamp and the reactor which contained the meteoritic samples were placed in a bigger chamber (grey box) to attain protection from radiation and ozone exposure.

3.2.1 Features of the irradiation reactor

Experiments were conducted in a leak tight, cylindrical reactor with a volume of 168 ml (diameter = 6.6cm and depth = 2.4cm). Its lower part contained two gas connections placed on opposite sides, an inlet and an outlet, which regulated the gas circulation inside the reactor. The meteorite sample was positioned inside the reactor, which was closed on top by a quartz plate (Suprasil). The transcendent purity of this silica made material in comparison to normal glass containing other ingredients, gives the Suprasil disk the physical property to be almost totally transparent to ultraviolet wavelengths between 280 – 400 nm. The disk was tightened on top with a silicon ring and a screwed cap. The effect of the quartz plate was measured during the calibration of the Xenon lamp and Waldmann UV meter. A sensor was attached to the outer part of the reactor to take continuous temperature measurements.

3.2.2 Xenon arc lamp

A Xenon arc lamp was chosen as a light source since it approaches the energy and abundance of photons (190 - 400 nm) arriving the Martian regolith (according to models). Other irradiation lamps like the ones functioning with mercury, deuterium or hydrogen produce an ultraviolet spectrum which is not closely related to the one produced by the sun (Poch et al., 2013).

The Xenon lamp spectrum extends beyond the UV range and also produces lower frequency photons from the infrared region up to 2200 nm. Experiments were carried out to check the molecular alterations of glycine under exposure to infrared radiation solely (that caused temperature variations of 2°C). It was revealed that infrared photons IR effects play an insignificant role on the destruction of organics (Poch et al., 2013), revealing that wavelengths beyond UV would not have a notable effect on the organics of the meteorite samples.

3.2.2.1 Light generation mechanism

A Xenon lamp uses a Xenon noble gas discharge to produce artificial light. The functioning mechanism of the lamp is based on ionizing the Xenon gas and converting it to a plasma at the cathode of the lamp. On their way from cathode to anode, accelerated free electrons collide with the Xenon ions and go to a higher energy state. When they return to their initial energy state they lose energy in the form of a photon ranging between ultraviolet to infrared wavelengths. The bright, white light that is generated is similar to the light emitted from the Sun.

The problem presented on using a Xenon arc lamp is the production of ozone, which is a toxic gas. Similarly to the chemical procedure occurring in the stratosphere, UV radiation (UVC) interacts with oxygen molecules (around the lamp), breaking each

one down into two atoms of oxygen (reaction 1). Free oxygen atoms collide with oxygen molecules, resulting in ozone generation (reaction 2).



On using a Xenon lamp, measures should be taken to prevent direct eye contact with the xenon light, exposure to ultraviolet radiation and any ozone inhaling.

3.2.2.2 Spectral calibration, effect of 45° mirror and Suprasil disk

To acknowledge the precise radiation intensities of each wavelength between 280 - 400 nm (UVB and UVA) that were produced by the Xenon lamp, a calibration of the light source was undertaken through the use of a photometer. The effect of the Suprasil disk (top of the chamber) and the 45° mirror on the Xenon light wavelengths was also determined.

The direct UV measurements, as well as the radiation values when a Suprasil disk or a 45° mirror is affecting the light beam, are given in *Table 2* and plotted in *Figure 4*. UVB and UVA measurements of *Table 2* are the sum of all radiation values between 290-314nm and 314-400nm respectively.

Table 2: Ultraviolet irradiation values in W/m² as they were measured by a photometer when the light beam of the Xenon lamp was i. headed directly to the sensor, ii. filtered through a Suprasil disk and iii. reflected through a 45° mirror. The two last columns denote the proportional radiative reduction of the UV components of the light source (in comparison with the direct value) due to the effect of the Suprasil disk and the mirror.

Radiative intensity (W m ⁻²)					
	Directly	through a Suprasil disk	through a 45° mirror	Reduction due to Suprasil	Reduction due to mirror
UVA (314 – 400nm)	29.3	26.7	16.0	8.7%	47.1%

UVB (280 – 314 nm)	5.1	4.5	2.0	10.7%	54.0%
UVA + UVB	34.4	31.2	18.0	9.8%	51.5%

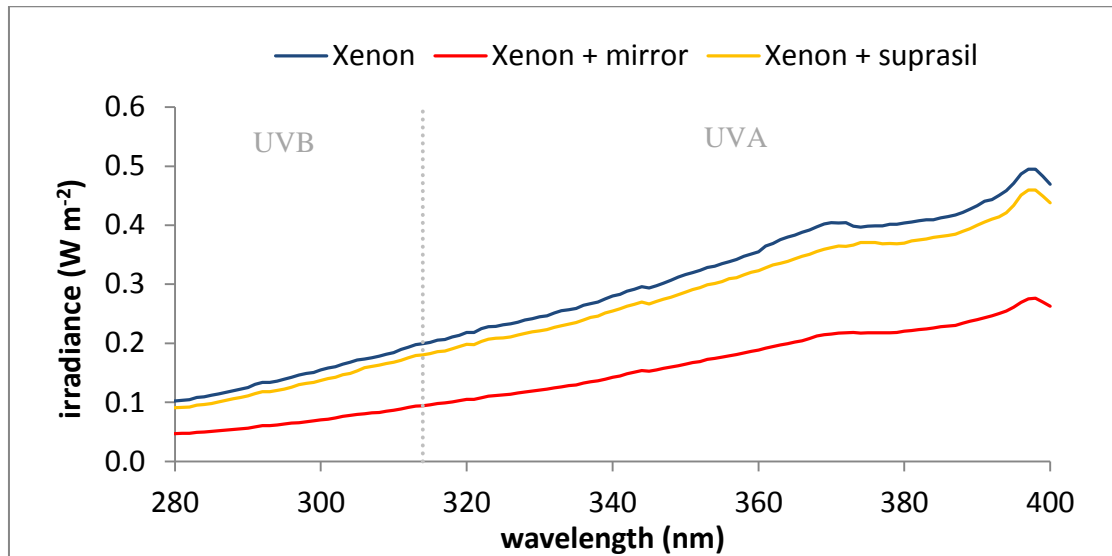


Figure 4: Spectral irradiance profile of the Xenon light for UVB (280-314nm) and UVA (315-400nm) in $W m^{-2}$. UV intensity measurements are shown by a blue line when the light beam was directed directly to the photometer, by a yellow line when a Suprasil disk was placed between the lamp and the photometer and by a red line when it was reflected by a 45° mirror.

Figure 4 reveals that when a Suprasil disk and even more notably when a mirror is imported in the system, it has a significantly reducible effect on every frequency of the UVA and UVB spectrum. Table 2 shows this trend in numbers.

The Suprasil disk affected UV wavelengths at a scale around 10%, for which UVA irradiance decreased down to 91% and UVB to 89%. The use of a 45° mirror leads to a reduction in ultraviolet wavelengths of the order of 50%. UVA irradiance was minimized by 47% and UVB by 54% in comparison with direct measurements. Both the mirror and the Suprasil disk were used simultaneously for the meteorite experiments. This decreased the direct Xenon UVA level by a factor of 0.56 and the UVB by 0.65.

3.2.2.3 Waldmann UV meter

Since the UVA and UVB intensity of each experiment was measured through a Waldmann UV meter (it does not have a UVC sensor), its calibration through the photometer (again including the effect of the mirror and the Suprasil disk) was also considered necessary. By knowing the relation between the value given by the UV meter and the real UV intensity, a Waldmann indication can be converted to the precise radiation value (real). During the calibration of the Xenon lamp (as shown in *Table 3*), measurements through the UV meter were also taken simultaneously. The first three columns in *Table 3* show the averaged indication for each case. The last two columns indicate the rate between the real UV intensity value (shown later on in the Results section) and the Waldmann indication.

Table 3: UVA and UVB indication values in Watts per area as they were measured by a Waldmann UV meter when the light beam of the Xenon lamp was i. headed directly to the sensor, ii. filtered through a Suprasil disk and iii. reflected by a 45° mirror. The last three columns show the rate between the real value (Table 2) and the Waldmann indication for the direct measurement, as well as when the Suprasil disk or the 45° mirror is interfering with the light beam.

Waldmann UV meter indications ($W m^{-2}$)						
	Directly	through a Suprasil disk	through a 45° mirror	Directly Real / Waldmann	Suprasil Real / Waldmann	mirror Real / Waldmann
UVA	21.6	20.2	15.0	1.4	1.3	1.1
UVB	5.4	4.9	3.3	0.9	0.9	0.6

By comparing the ultraviolet component values of *Table 2* (real) and *Table 3* (Waldmann), it is concluded that the UV meter is overestimating UVA and underestimating UVB for each case. More precisely, the real intensity of UVA (UVB) is 1.3 (0.9) times higher (lower) than Waldmann indication under the effect of Suprasil and 1.1 (0.6) times higher (lower) mirror.

The values in Table 3 were used to correct both types of experiments (i.e. methane emission and target irradiation) to calculate the real UV exposure of the meteoritic

material. For methane emission experiments 1 – 4 the mirror and the Suprasil effect were present. Since the Waldmann indication was taken only under the effect of the mirror, it acquired further reduction to add the Suprasil effect. To calculate the real UVA and UVB intensity, the final Waldmann value was multiplied by the factors shown in *Table 3* corresponding to the Real/Waldmann rates for the Suprasil and the mirror according to:

$$UVA_{real} = 1.3_{suprasil} \cdot 1.1_{mirror} \cdot (W_{mirror} \cdot 0.91) \rightarrow UVA_{real} = 1.43 \cdot UVA_{Waldmann}$$

$$UVB_{real} = 0.9_{suprasil} \cdot 0.6_{mirror} \cdot (W_{mirror} \cdot 0.89) \rightarrow UVB_{real} = 0,54 \cdot W_{final}$$

3.2.3 Picarro Fast CO₂/CH₄/H₂O analyzer

The Picarro analyzer is based on cavity ring-down spectroscopy (CRDS) technology to take simultaneously precise measurements of carbon dioxide, methane and water mole fraction.

3.2.3.1 Cavity ring-down spectroscopy

CRDS is a highly accurate technique in measuring the progressive loss in light intensity due to the radiative absorption and scattering physical properties of an imported gas sample. Almost each gas-molecule has a unique absorption spectrum as a function of frequency. Methane strongly interacts with specific wavelengths from the infrared region at 1400nm and 2600nm, which is utilized to determine its mixing ratio. The absorption of radiation by trace gases is relatively low, which restricts the ability of common spectrometers to part per million levels. This limitation is exceeded by CRDS technology by increasing the pathlength up to a few kilometers and allowing the sensitivity to reach part per billion values (1000 times more accurate than conventional spectrometry) (Lehmann et al., 2009).

The mechanism behind the CRDS is based on a single frequency laser beam that is introduced in a cavity and is reflected among mirrors (Picarro has three mirrors). Since their reflectivity is a bit less than 100% (99.999%) any radiation leakage is tracked by a highly sensible photodetector. When the leak indication reaches a certain value (in microseconds), the laser is turned off. The light continues to be reflected inside the cavity ($\approx 10^5$ times), while its intensity decays exponentially down to zero. This results into a laser travel distance of over 20km, despite the 25cm distance between mirrors. The time interval for the decay is called *ring down time*.

In case of an empty cavity, the ring down time is only mirror reflectivity dependent. When a gas sample (whose absorption wavelengths are in the range of the laser spectrum) is inserted inside the cavity, the factor of radiation absorbance increases and the ring down time decreases. Picarro can compare the ring down time with/without gas specie inside the cavity, by switching the laser from a wavelength that doesn't interact with the target gas to one that is strongly absorbed by it. By estimating this difference the mixing ratio of the sampled gas can be quantified (Lehmann et al., 2009).

In the context of this project, the Picarro analyser was set to mode 1 that measures methane mixing ratios at a rate of 10Hz. The used laser emits a light beam of wavelength equal to 1603 nm, which is strongly absorbed by methane molecules.

3.2.3.2 Calculations

The Picarro analyzer calculates automatically the mixing ratio of the sample gas according to the following mathematical functions. The light intensity of the mirror-attached photodetector is

$$I(t, \lambda) = I_0 \cdot e^{R(\lambda) \cdot t}$$

for which I_o is the laser intensity when light was turned off and $R(\lambda)$ is the optical decay constant which depends on wavelength. When a gas that absorbs at the specific wavelength enters the cavity then optical losses increase and thus ring down times decrease (decay is faster). The loss rate for a particular wavelength when cavity is empty / filled with gas are given by

$$R(\lambda, 0) = \frac{1}{\tau(\lambda)}$$

$$R(\lambda, C) = R(\lambda, 0) + c \cdot \varepsilon(\lambda) \cdot C$$

where $\tau(\lambda)$ is the ring down decay time, c is the speed of light, $\varepsilon(\lambda)$ is the extinction coefficient and C is the concentration of the introduced gas. The value of the extinction coefficient and the concentration of the gas can be calculated by taking the ratio between the decay constant of an empty chamber (τ_o) and a chamber filled with gas (τ):

$$\tau_o = \frac{n \cdot l}{c \cdot (1 - R(\lambda, 0))}$$

$$\tau = \frac{n \cdot l}{c \cdot (1 - R(\lambda, C) + \alpha l)}$$

for which n is the refraction index in the cavity, l is the length of the cavity and α is the absorption coefficient for a specific wavelength.

To estimate the magnitude of the total pathway travelled by the light, ring down time must be multiplied with the speed of light

$$L = c \cdot \tau(\lambda)$$

3.2.4 Methane emission experiments

When starting an experiment the reactor was flushed with normal compressed air at a rate of 70 ml/min, whose methane consistence was constant for a certain gas cylinder. The flow rate of the gas was regulated by two mass flow controllers, MFC1 and MFC2. The mixing ratio of methane was measured every second by a Picarro analyzer with precision of ± 1 ppb. A vent was placed before the outflow of the reactor and the Picarro to prevent overpressure to occur. Between the MFCs and the reactor, a Valco two position valve was installed. The time interval of switching between the positions could be selected by the analyzer. When switching from one valve position to another, measured methane mixing ratio was either deriving from the reactor (position 1) or directly from the gas bottle (position 2). During position 1, 70 ml of gas per minute were flushed through MFC1 to the reactor and onwards to the Picarro analyzer, while the gas passing through MFC2 was flushed out of the set up. When the system shifted to position 2, MFC1 flushed the gas directly to the analyzer while MFC2 entrained the bottle gas through the reactor (at a rate of 50 ml/min) that eventually went out of the system. In case that accumulation of produced meteoritic methane was desired during position 2, a valve placed between MFC2 and the reactor was switched to stop the flow.

An Osram 450W Xenon lamp was used as a source of ultraviolet radiation. The voltage of the lamp was set at 17V and the current at 23.1A. The light beam was guided directly over the exposed meteoritic material through a reflecting mirror angled at 45°. Initially the reactor was placed at a distance of 35 cm from the mirror (from the bottom of the reactor until the bottom of the mirror). The radiative intensity of the light source was later diminished by augmenting the reactor/mirror distance or by decreasing the focus level of the beam (through an established lever).

3.2.5 Blank measurements

Before starting irradiation experiments, blank measurements were performed to quantify and exclude any methane emissions from materials other than meteoritic grains. A petri dish which would be used to hold the meteorite sample was cleaned (with milliQ water, acetone and ethanol) and placed in the oven at 250°C for 1 hour. The cleaned dish was put inside the reactor. Then the chamber was flushed with normal air gas from a high pressure cylinder and the setup was exposed to UV radiation for a specific time interval (same conditions as a methane emission experiment, but without meteorite material). Two different cylinders with different CH₄ mole fraction were used, so two blank tests were performed for each used background gas. During irradiation, the system switched every few hours to the accumulation step for 20-30 minutes to check the stability of the flushing gas.

3.2.6 Gas stability measurements

Every time a new gas cylinder was attached to the system, its methane mixing ratio stability needed to be confirmed prior to the beginning of any experiments. The setup was set to mode 2 to allow the analyzer to take direct measurements from the gas source for a few hours. Before the initiation and after the ending of each experiment, the stability of the methane supply cylinder was checked for 30 minutes. In case the experimental period exceeded a few hours, then the system was set to switch every few hours to mode 2 for 25 – 30 minutes to take measurements of the cylinder gas.

3.2.7 Irradiation of meteorite samples

The first category of experiments was to investigate methane emission sourcing from meteoritic material during ultraviolet interactions and it comprised of experiments 1-4. A Mettler H10T Analytical Balance of readability up to 0.1mg was used for precise mass measurements. As shown in *Table 4*, for experiments 1, 2, 3 and 4: 95.8mg,

92.3mg, 99.9mg and 101.6mg of grained meteoritic material sized around 100 μ m were used respectively. The grains were distributed on a sterilized petri dish in a circular area (which covered around 2.5 cm² for experiment 1-2, 3 cm² for experiment 3 and around 6 cm² for experiment 4) and they were placed inside the reactor. The chamber was flushed with the cylinder gas at a flow rate of 70 ml min⁻¹. After determining the methane mole fraction of the incoming air for one hour, the chamber was exposed to ultraviolet radiation for a specific time interval.

To check the effects of exposing the material to different UV conditions, the distance between the sample and the bottom of the Xenon lamp mirror was varied. For experiment 1 it was at 35cm (5cm of reactor depth + 30 cm from top of the reactor until the mirror bottom,) while for experiment 2 this distance was 50cm. For experiment 3 and 4 the reactor/mirror distance was set at 35cm, but the light beam was altered to be less focused. Ultraviolet levels were measured with the Waldmann UV meter at the beginning and the end of each experiment and their average is shown in Table 1 (corrected measurements according to the calibrated data). By moving from experiment 1 to 4, UVA and UVB intensities were decreased. For experiment 1, UVA and UVB were around eleven and six times respectively higher than modeled Martian radiation conditions. During experiment 2 the UVA level was 55% lower than experiment 1, while UVB intensity was 62% lower. Radiation levels that were applied for experiments 3 and 4 were similar to the values used by *Kepler et al (2012)*, but closer to the UVB values indicated by Cockell (Cockell, 2000) for the Martian surface near the equator. *Table 4* gives the UV irradiances of each experiment in Watts per m².

Table 4: UVA and UVB irradiation time (h) and intensity for methane emission experiments 1 – 4. The mass (mg) of each meteorite sample and the surface area it covered (cm²) is also given. The mass to exposed surface ratio is noted in the last row. Ultraviolet values used by Kepler et al. (2012) and the model calculated values for the surface of Mars around the equator by Cockell (2000) is also noted.

Experiment					
1	2	3	4	Kepler	Mars

Exposure time (h)	96	48	72	96	-	-
UVA (W/m²)	420.5	188.7	38.7	33.5	36.3	35.6
UVB (W/m²)	48.0	17.9	5.4	4.5	4.8	8.6
mass (mg)	95.8	92.3	99.9	101.6	200	-
area (cm²)	2.5	2.5	3.0	6.0	-	-
ratio (mg cm⁻²)	38	37	33	17	-	-

Because the emission rates measured directly were rather low (few ppb only), most experiments were carried out as a mixture of “accumulation experiments” and “online experiments”. During the “accumulation period”, the flow through the reactor was stopped for a certain time to allow methane to accumulate in the chamber. During this time the incoming gas was measured by the Picarro instrument. After 25 minutes, the accumulated methane was flushed with the cylinder gas into the Picarro analyzer. It appears in the instrument as a large methane peak. For calculation of the emission rate, the area under the accumulated peak was then integrated, and the methane released was “distributed” over the accumulation period. After the peak has been detected, the measurement was continued “online” to see directly the signal from the irradiation chamber. The online signal was compared to the accumulation signal to avoid biases from the small signals.

3.3 UV penetration experiments

3.3.1 Targets (preparation and irradiation)

The aim of the second category of experiments was to investigate the carbon balance after UV photons have penetrated the meteorite matrix and interacted with present organic material (which resulted the methane emission recorded during experiments 1 – 4). The solid meteorite fragment was crashed into smaller pieces. Seven segments that possessed a size around 1 – 2 mm were collected. Each of them was embedded in a target holder (a carbon sticker of 10mm surrounded by a plastic ring) and then it was filled with resin that was left to cool and solidify (*Figure 41a – b*). The purpose of

the carbon tape is to hold the material in place, while resin is poured around it. The target was polished with a polishing wheel at the side of the meteorite fragment until the carbon tape was completely removed. One target was kept as blank, while the remaining six were later on irradiated to be used further on for SEM and NanoSIMS analysis.

Table 5 shows the UVA and UVB intensities that were applied to each target.

Table 5: UVA and UVB irradiation levels for high and low exposure targets. Four targets were irradiated under low irradiation UV (approaching UVB of Cockell) for 6, 12, 24 and 36 hours and 2 targets under higher ultraviolet light for 24 and 72 hours.

Targets	Irradiance (W m^{-2})	
	Low UV radiation 6h, 12h, 24h, 36h	High UV radiation H24h, H72h
UVA	56.8	139.5
UVB	7.9	18.1

The first 4 targets were irradiated with a UVB intensity that was almost a replica of the one given by Cockell (2000, Table 4) for the surface of Mars (latitude = 0° - 20°). The irradiation time of each target was decided after checking the methane mass production values of the first set of experiments (experiment 1-4). Low irradiation targets were exposed under UV radiation of UVA = 56.8 W m^{-2} and UVB = 7.9 W m^{-2} , which approximated UVB conditions on the surface of Mars. Irradiation periods for each target were set at 6h, 12h, 24h and 36h, which corresponded to approximately 20%, 40%, 60% and 80% of total methane production ($\mu\text{g m}^{-2}$) for the first 48 hours of methane emission experiments 1 – 4 (see below). To check the effect of UV intensity on the achievable penetration depth under the meteorite surface, targets 6 and 7 were irradiated under approximately double UV values. They were exposed to UVA = 139.5 W m^{-2} and UVB = 18.1 W m^{-2} for 24 and 72 hours. The decision to irradiate target 6 for 24 hours was taken because the CH₄ emission experiments indicated that

approximately 50% of the total methane emitted after 72 h under these luminosities (target 7) was released after 24 h.

3.3.2 Scanning electron microscopy (SEM)

Information about the chemical composition of the targets near the surface was obtained by applying SEM analysis to the targets. SEM technology uses an electron beam that is directed towards a specimen's surface. When it hits the surface, a fraction of the high kinetic energy electrons is decelerated and a large proportion of their energy is transferred to the molecules of the sample (down to about 1 μ m depth). This causes the emission of a secondary signal originating from the material which consists of secondary electrons, backscattered electrons, diffracted backscattered electrons, photons (X-rays and visible light) and heat. Secondary electrons are detected and analyzed to produce a two dimensional image of the surface morphology of the sample (SEI image).

When the accelerated electrons hit the sample, a series of elastic and inelastic collisions occurs between electrons and atoms. During elastic collisions, the trajectory of the incident electron beam changes, but their kinetic energy is maintained. The chance of an elastic backscatter collision increases as the size of the collided atom becomes bigger (larger cross-sectional surface area). Therefore the higher the intensity of the detected backscattered electrons (BSE, measured by a BSE detector) the larger the atomic number of the atom they interacted. The BSE produces a two dimensional image, where darker areas correspond to lower backscatter thus lower atomic number, and lighter areas to higher backscatter and thus higher atomic number. Conclusions about the chemical composition of a sample can be derived by studying these images.

An energy dispersive detector (EDS) was also used analyze the X-ray signal deriving from the material. Each element has a different, characteristic energy spectrum which can be analyzed by the EDS to distinguish the identity and abundance of the various

elements in the sample. The result is a plot of x-ray number of measurements as a factor of energy (which is unique for each element). A 2D elemental map showing the distribution of C, Fe, O, Si, S, Ca and Mg was produced.

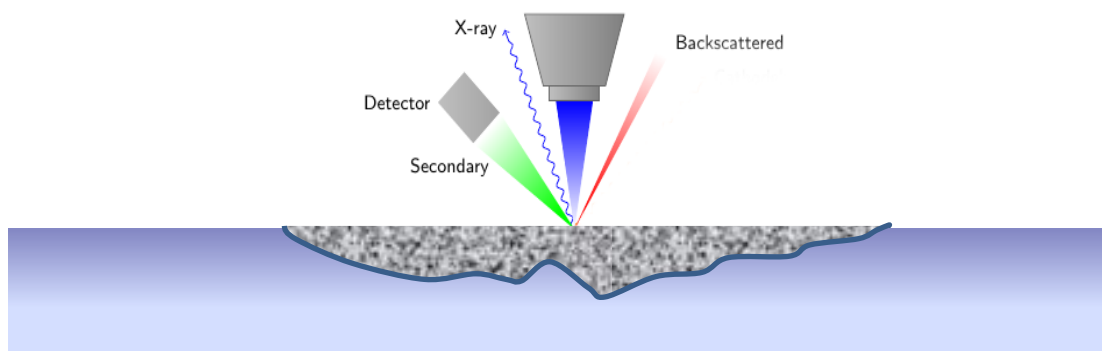


Figure 5: Illustration of SEM analysis (<http://www.texample.net/tikz/examples/scanning-electron-microscopy>) on a meteorite target. Emitted secondary electrons produce topographic images, backscattered electrons result in atomic number images while x-ray detection creates elemental maps.

3.3.3 NanoSIMS

A secondary ion mass spectrometer (SIMS) is an ion microprobe that provides accurate information about the molecular resolution and isotopic composition of a material. This technique can be applied to the surface of the sample, as well as to layers beneath. The process starts with the bombardment of the sample with charged particles (primary ion beam: Cs^+ or Ga^+) at a continuous, steady rate. This will cause the ejection of secondary ions from the incident surface, which are directly removed by an immersion lens (secondary beam). To maintain a steady secondary ion beam current, the charge of the sample surface should be unaltered so that its potential difference with the immersion lens remains fixed. To accomplish that, the targets were coated with a 5nm layer of gold which removed any charging of the sample. The secondary beam transfers different energy ions to a magnetic analyzer to be separated into lower and higher charged particles. Then according to their mass-to-charge ratio they detected by a mass spectrometer.

For the analysis of the targets, areas of $15 \times 15 \mu\text{m}^2$ were analysed. NanoSIMS was applied at locations that were chosen according to the SEM elemental maps that

revealed the possible presence of specific minerals. The depth resolution was not known because these were the first mineral samples to be analysed with the UU nanoSIMS.

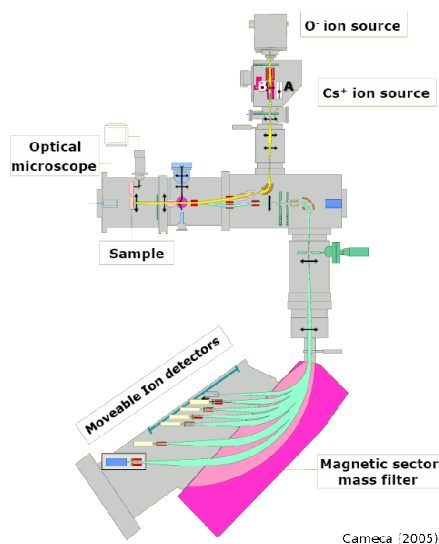


Figure 6: An illustration of the Secondary ion mass spectrometer. The sample is shot at a specific spot with Cs^+ ions at a steady state. Secondary ions that are ejected from the specimen surface are directed to a magnetic sector mass spectrometer to be separated according to their mass to charge ratio (Cameca, 2005).

3.3.4 Calculating the emission rates

Methane mixing ratio measurements of the Picarro analyzer can be converted to methane mass emission per time. The following formula was used to calculate the emission rate of methane [ngCH_4/min] sourcing from the irradiated meteoritic material

$$ER = \frac{f \cdot \Delta C \cdot M_{\text{CH}_4}}{M_{\text{air}}}$$

where f is the flow rate ($70 \text{ ml} \cdot \text{min}^{-1}$), ΔC is the measured mixing ratio change (in ppbv), M_{CH_4} is the molar mass of methane ($16 \text{ g} \cdot \text{mol}^{-1}$) and M_{air} is the molar mass

of dry air per 1000 ml of air ($24,04 \text{ l}_{air} \cdot \text{mol}_{air}^{-1}$) both at a specific constant temperature (20°C), and DW is the dry weight of the meteorite sample (around 0,1 g).

The ΔC is calculated by subtracting the averaged value of the blank from the measured averaged mixing ratio of the sample for a specific time period (every hour)

$$\Delta C = C_{averaged/sample} - C_{blank}$$

The flow rate level is crucial in determining the minimum tractable ΔC value by the analyser. If the flow rate is very high then the emission signal ΔC for a given emission rate ER might be non-detectable or confoundedly weak. On the contrary, when the reactor is flushed at a relatively slow rate the contained produced methane is allowed to increase which will eventually give a larger measured mixing ratio change.

By multiplying the ΔC value with the f/M_{air} (mole of air passing through the reactor per minute), the mole of meteoritic produced methane per minute is acquired. The emission rate resulting from $ER = \frac{f \cdot \Delta C \cdot M_{CH_4}}{M_{air}}$ is in $ng_{CH_4} \cdot min^{-1}$.

The used meteorite mass and exposed surface to irradiation differed between samples. To be able to compare the results among experiments, emission rates were normalized per mass and per surface area. The two emission rates calculated for each sample were

$$ER = \frac{f \cdot \Delta C \cdot M_{CH_4}}{M_{air} \cdot DW}$$

$$ER = \frac{f \cdot \Delta C \cdot M_{CH_4}}{M_{air} \cdot A_{sample}}$$

where DW was the dry weight of the meteorite sample (around 0,1 g) and A_{sample} the exposed meteoritic surface. The unit of the emission rate normalized per dry weight and surface area was $ng_{CH_4} \cdot g_{sample}^{-1} \cdot min^{-1}$ and $\mu g_{CH_4} \cdot m^{-2} \cdot min^{-1}$.

3.3.5 Calculating the penetration depth from the emission rate values

By calculating the area under the plot of the emission rates, the total produced methane mass can be specified according to the trapezoidal rule. The area between two continuing emission rate values is found by multiplying their sum by the time interval between them and dividing by 2.

Since the density (Keppler et al., 2012) of the meteorite ($\rho = 2,85 g \cdot cm^{-3}$), the mass and the exposed surface for each experiment is known, the thickness (h) of every sample can be estimated in nanometers (assuming that all the grains are well distributed side by side) according to

$$h = \frac{m}{\rho \cdot A_{sample}}$$

Approximately 2% of carbonaceous chondrites is made of carbon, thus by multiplying the sample mass with 0.02 will give the carbon mass that is expected in the used material. By dividing this value by the depth of the sample (h), the carbon content per nanometer layer of the meteorite can be estimated. Assuming that all carbon is removed from a nano-layer before photons can go deeper, the achievable penetration depth for a specific methane mass production (found from the emission rate) can be calculated.

4 Results

4.1 Instrument stability

Two different gas cylinders were used for the methane emission experiments. They contained compressed normal air and their methane mole fraction is shown in

Table 6.

Table 6: Methane mixing ratio of cylinder 1 (for experiment 1) and 2 (for experiment 2, 3 and 4) as it was measured from the control checks before/after/during experimental run.

CH ₄ mixing ratio (ppmv)		
Cylinder	1	2
	(exp. 1)	(exp. 2 – 4)
Average	2.0072	1.9282
St. deviation	0.0008	0.0009

To exclude any methane mixing ratio perturbation effects of the flushed gas during experiments, the stability of the instrument was checked and confirmed before the initiation and after completion of each experiment. Due to the long running time of meteorite experiments (up to 96 hours), background gas constancy with respect to CH₄ was also measured every 2 hours by switching the valve of the system to mode 2 (cylinder gas flushed directly to the analyser) for 30 minutes.

Figure 7 shows the 4 – hour methane mixing ratio stability measurement of the incoming gas from the first cylinder (which was used for meteorite experiment 1) prior to the experiment.

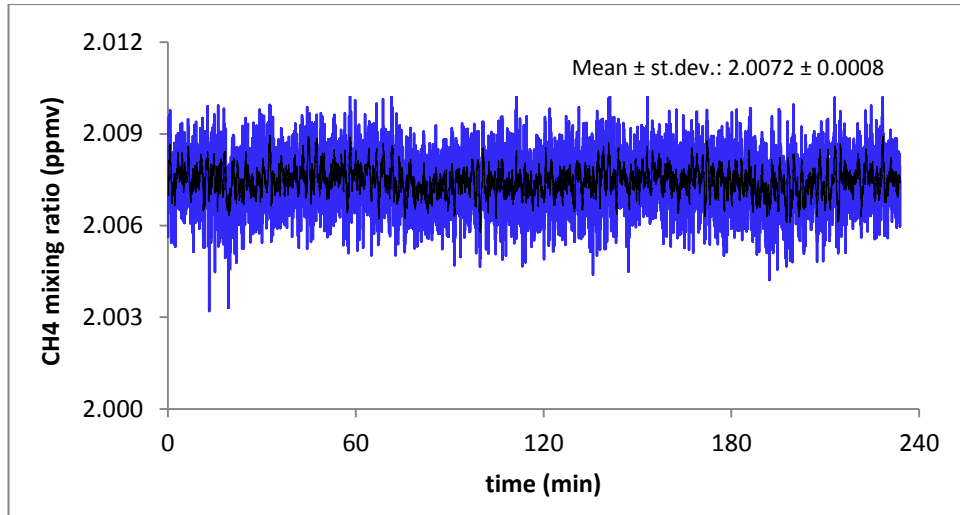


Figure 7: Stability of the flushing gas (normal air) for 240 minutes of measuring (lamp was off). The blue line shows the raw data as measured by the Picarro analyzer per second, which were averaged per 10 seconds (black line).

The mole fraction of methane remained relatively stable in time and acquired a mean value of 2.0072 ppmv with a standard deviation of 0.0008 ppm. To check how the data are distributed around their average value, measurements were divided into bins equal to one fourth of the standard deviation (1 bin = 0.2 ppb). *Figure 8* shows the resulting bins in a probability density function plot.

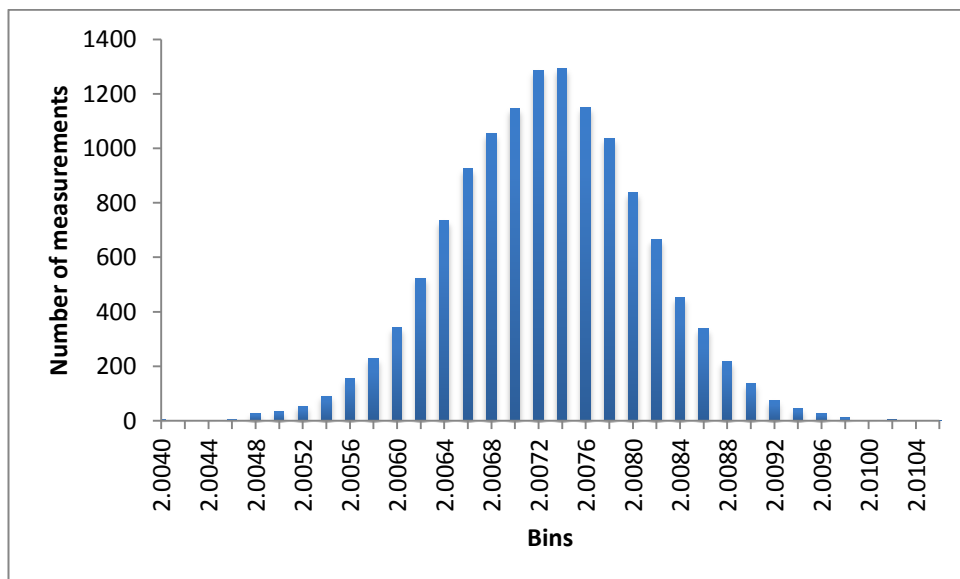


Figure 8: Probability density function of the stability check measurements of flushing gas sourcing from cylinder 1 (1 bin = 0.2ppb = $\sigma/4$)

Methane mixing ratio values follow a Gaussian (normal) distribution around the average value. The same test was repeated for the second cylinder (used for meteorite experiments 2 – 4), whose methane constitution was lower than cylinder 1. It showed a mixing ratio of 1.9282 ± 0.0009 ppmv.

4.2 Blank measurements

Since methane emission experiments were divided into higher and lower UV intensity (Mars like) experiments and two different gas cylinders were used, two blank measurements were taken under two different irradiation intensities. The background gas of experiment 1 was used for the first blank measurement. It lasted 24 hours and was conducted under $UVA = 170 \text{ W m}^{-2}$ and $UVB = 17 \text{ W m}^{-2}$ exposure. For the second blank measurement, the used flushing gas was the same as the one used in experiments 2 – 4. It was conducted for 96 hours (to ensure its stability after long term UV exposure) and irradiation intensity was set much lower; $UVA = 28.3 \text{ W/m}^{-2}$ and $UVB = 3.9 \text{ W/m}^{-2}$ (Mars like value). *Table 7* shows the mixing ratio of methane of the incoming/outgoing gas to/from the reactor and the resulting blank signal.

Table 7: Methane mixing ratio (ppmv) of the flushing gas (incoming) and outgoing gas for blank experiments 1 and 2. The difference increase in mixing ratio gives the blank signal.

Mixing ratio (ppbv)			
Blank	Incoming gas	Outgoing gas	Blank signal
1	2007.6	2008.7	1.1
2	1928.2	1928.8	0.6

The nominal mole fraction of CH_4 in the first cylinder (measured as the incoming air) was 2007.6 ± 0.8 ppbv. After being flushed through the irradiated reactor, the mole fraction increased to 2008.7 ± 0.8 ppbv, indicating a blank signal of about 1 ppb. Concerning blank 2, the incoming gas (into the reactor) had an average methane

value of 1928.2 ± 0.9 ppbv and the outgoing gas (out of the reactor) 1928.8 ± 0.9 ppbv, showing a blank value of 0.6 ppbv that remained relatively stable during the whole experimental period (4 days). Decrease in irradiation intensity (from blank 1 to blank 2) had a small effect on the blank signal. For experiments 1 – 4 the blank signal varied between 0.6 and 1.1 ppbv.

In *Figure 9* the first 24 hours of the second blank measurements are shown. Every 4 hours of measuring, the system shifted for 25 minutes to mode 2 (accumulation phase), which is indicated in the chart as a grey area. This was done to check and confirm the stability of the flushing gas in respect to its methane constitution.

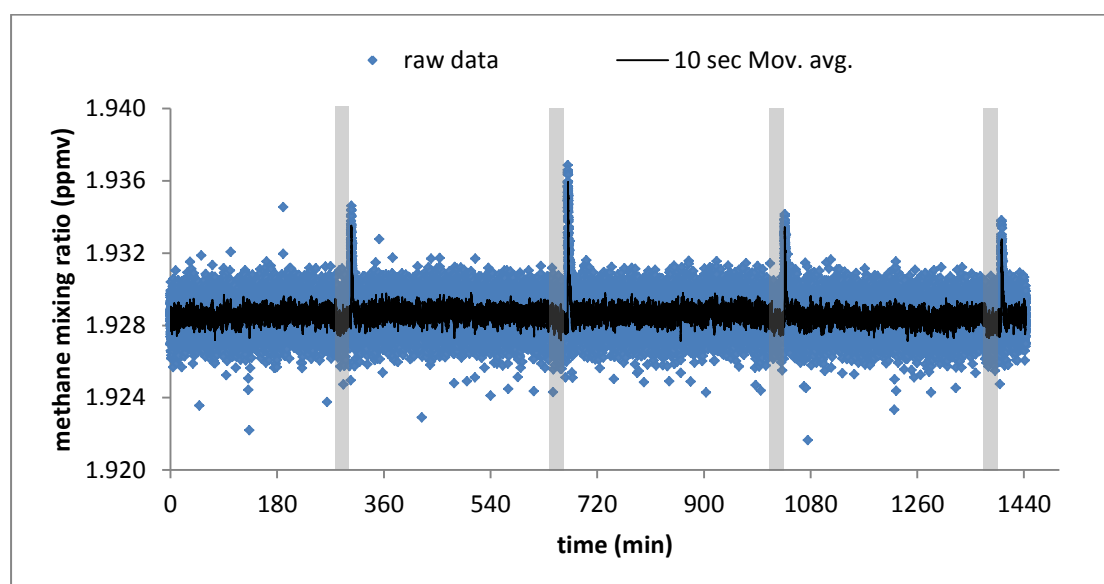


Figure 9: First 24 hours (out of 96 hours) of blank measurements for experiment 2-4. **Blue spots** represent the raw data measured per second by Picarro analyzer, which were smoothed by using a 10 seconds moving average (black line). Every 4.5 hours the system switched to accumulation mode for 25 minutes (**grey areas**) to check methane mixing ratio stability of the background gas (1928.2 ± 0.9 ppbv).

Figure 10 illustrates a typical peak of the time series (2nd peak of *Figure 9*). The system switched to accumulation time (645 – 670 min), so that the cylinder gas was flushed directly to the analyzer and its methane mixing ratio was measured. Since no gas flow was conducted in and out of the reactor (irradiation was continuous in both mode 1 and 2), methane deriving from the blank was allowed to accumulate. When the system returned to mode 1 (≈ 670 min) and air started flowing through the reactor, a

methane peak appeared as a result of 25 minutes of accumulation (green area). By calculating the area between the peak and the average methane mixing ratio (gas + blank), blank methane production corresponding to 25 minutes of accumulation can be acquired.

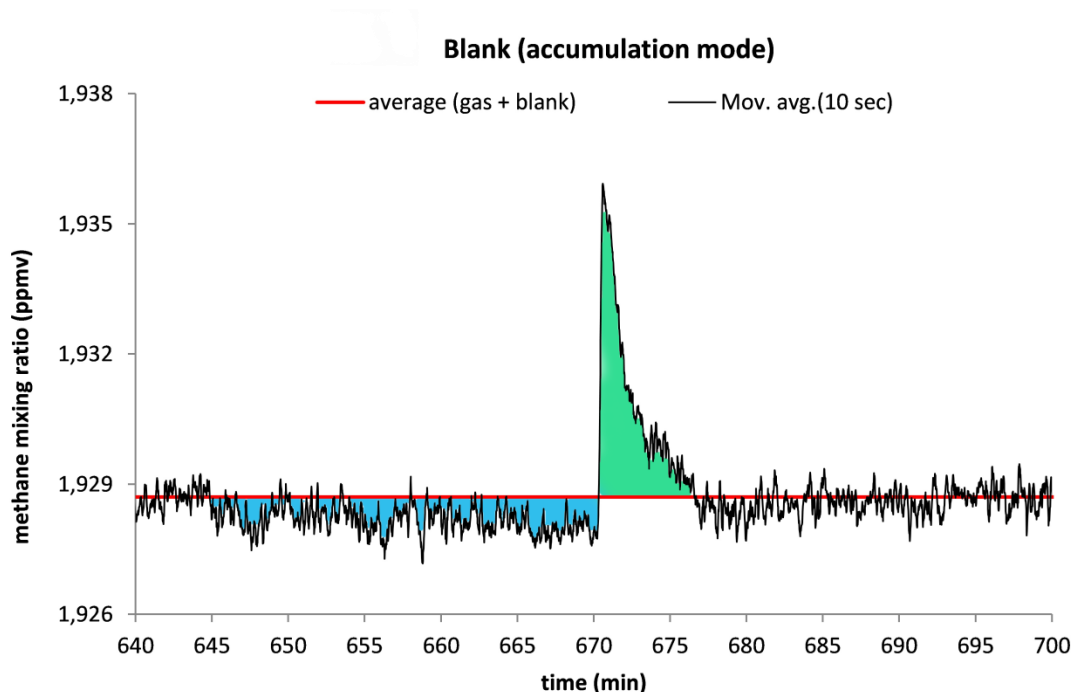


Figure 10: Example of an accumulation period. The system switched to mode 2 (accumulation) at 645 min and returns to mode 1 after 25 minutes, at 670 min. The red line shows the average methane mixing ratio when the reactor was irradiated with UV and flushed with normal gas deriving from gas cylinder 2 (CH_4 mixing ratio = 1928.2 ± 0.9 ppbv). The green area shows the extra methane production during accumulation time, while the blue area denotes the lack in methane mixing ratios when the blank effect is removed.

For blank experiment 2, each area under the peaks varied between 12 – 20 ppb * min and it was on a similar scale as the difference between the average methane mixing ratio (gas + blank) and the gas mixing ratio (1.9288ppmv), which is shown as a blue area in *Figure 10*. This proves that no leaks in or out of the system were present and that the increasing methane signal (in comparison with the cylinder methane values) is due to the interaction of the flushing gas with the UV irradiation inside the reactor. When produced methane during mode 2 (12 – 20ppbv) is divided by the accumulation time (25 minutes), the attained value varies between 0.5 – 0.8 which is in agreement

with the blank signal shown in *Table 7*. The same calculations were repeated for the accumulation peaks of blank 1, which gave similar results.

To check whether the blank measurements are also normally distributed, their probability density function was plotted and is shown in *Figure 11* for blank 2 (measurements were divided into bins equal to half standard deviation ($1 \text{ bin} = 0.5\sigma = 0.45 \text{ ppbv}$)). To better visualise the dispersion of the data, a Tukey box plot is also presented in *Figure 11*. The values of the first and third quartile (Q1 and Q3) represent 25% and 75% of the total measurements respectively. The interquartile range (IQR) shows the range at which 50% of the data are distributed. According to Tukey, the extension of the whiskers is defined at a distance equal to $1.5 \cdot \text{IQR}$ (one and a half times of the 50% of the measurements which are around the mean) from quartiles 1 and 3. Any values outside this range are considered as outliers and are not taken into account.

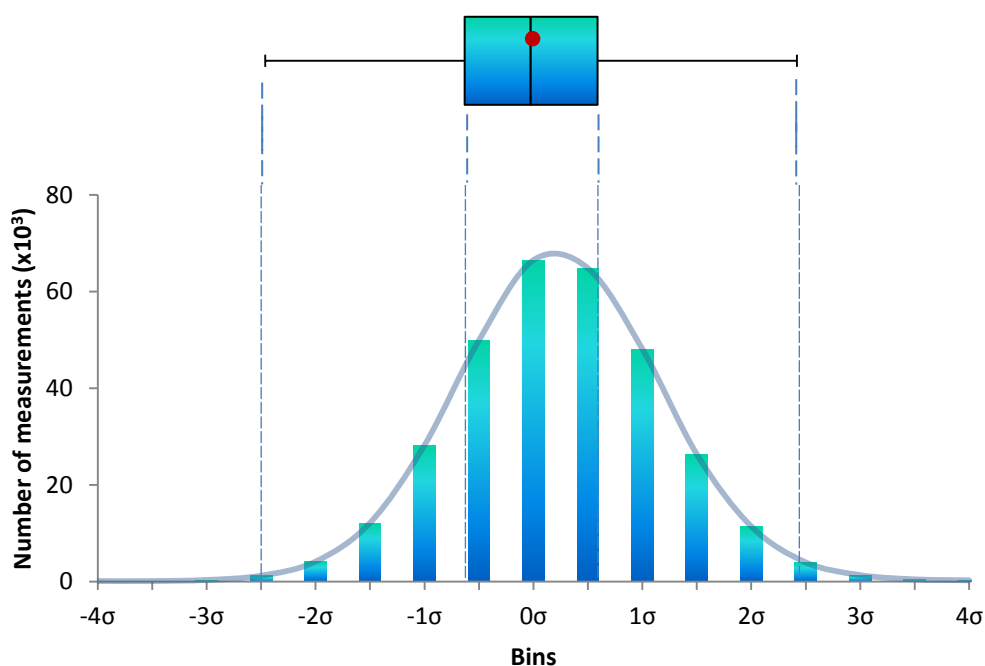


Figure 11: Probability density function of blank experiment 2 for 96 hours of measurements. Data values were divided into bins equal to one half standard deviation ($1 \text{ bin} = 0.5\sigma = 0.45 \text{ ppb}$). The y-axis shows the measurement count in thousands for each bin. The grey line shows the Gaussian distribution of the data. On the top, a box plot shows quartiles 1 and 3

(IQR = Q3-Q1), the median, the mean (red dot) and the whiskers ($Q1 - 1.5 \cdot \text{IQR}$, $Q3 + 1.5 \cdot \text{IQR}$) of the measurements.

The plot reveals that half of the measurements are under $\pm 0.5 \sigma$, showing the large distribution of the data close to the average value. The derived blank signal is relatively small and steady in time, showing that the petri dish and flushing gas under ultraviolet irradiation can't interfere with measured methane mixing ratios by a value higher than 1.1 ppbv. It also shows that the error is dominated by a random error in the measurement setup itself (likely the Picarro itself) and not a systematic effect (for example a change of the blank with time).

4.5 UV intensity of experiments

Figure 12 illustrates the UV irradiance spectrum that the targets in methane emission experiments 1 - 4 were exposed to. The shown values were calculated by scaling the spectra obtained during the lamp calibration by the measured radiation values of the Wanlmann device (see section). They are also compared with the modelled UV spectrum of the Martian surface at 20° latitude with dust density $\tau = 0.1$, as it was calculated by Cockell (Cockell, 2000).

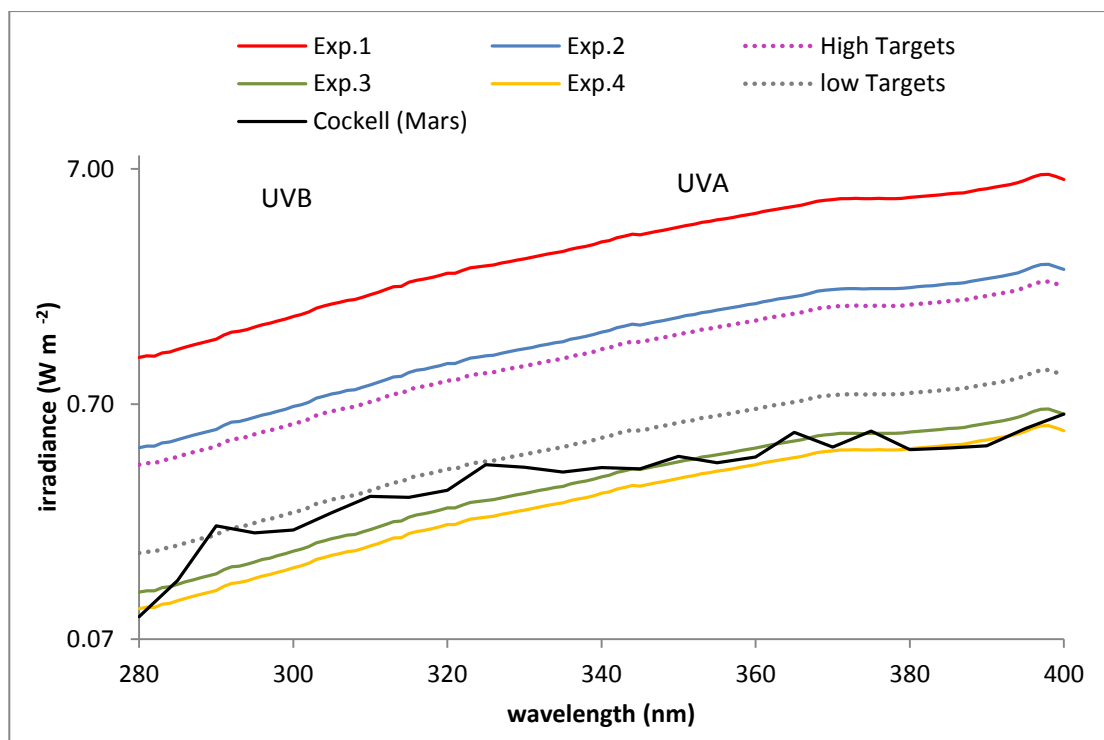


Figure 12: Spectral irradiance of the Xenon light used in each experiment. The y-axis is on logarithmic scale and denotes the irradiance of each wavelength between 280 – 400 nm (UVB and UVA), corrected for the effect of the 45° mirror and the Suprasil disk. Continuous lines show methane experiments 1 – 4, while dotted lines correspond to high/low irradiation targets experiments. The black line shows the corresponding Martian UV irradiance, as it was calculated through modelling by Cockell (at a latitude of 20° and dust loading $\tau = 0.1$ optical depth).

4.6 Methane emission experiments 1 – 4

4.6.1 Methane mixing ratios

The Picarro analyzer calculated 14 to 16 methane mixing ratio values every second. This resulted in massive data files for the corresponding experimental periods, which needed to be significantly reduced. The mixing ratio of data within each second varied at a scale lower than 1 ppb. Thus only one random measurement was kept for each second while the rest were removed, resulting in a fifteen times reduction of the data files. Subsequently, the blank was subtracted from the measurements (section 4.3) and the hourly averaged value was calculated, which induced the removal of accumulation drops and peaks from the final plots.

To further explain the data analysis method, an example is given in *Figure 13* which shows the raw results (pink line) for the first 24 hours of irradiation of experiment 2. When the pink line measures the incoming air (1928 ppb), the reactor is in accumulation mode. After that, the accumulated methane peaks are injected (off scale) and then the system returns to the “online” measurement, where the plateau indicates the instantaneous increase of CH₄ relative to the incoming air. The red line shows the hour averaged evolution of these plateau values (the data after the accumulation period and the 10 minute decay period right after the peak). The grey time series shows the blank measurements (also in accumulation mode) for the same time interval. The blue line shows the difference between the meteorite irradiation experiments and the blank experiments. The methane emission signal decreases from 7.3 ppb in the beginning to 1.7 ppb after 19 h.

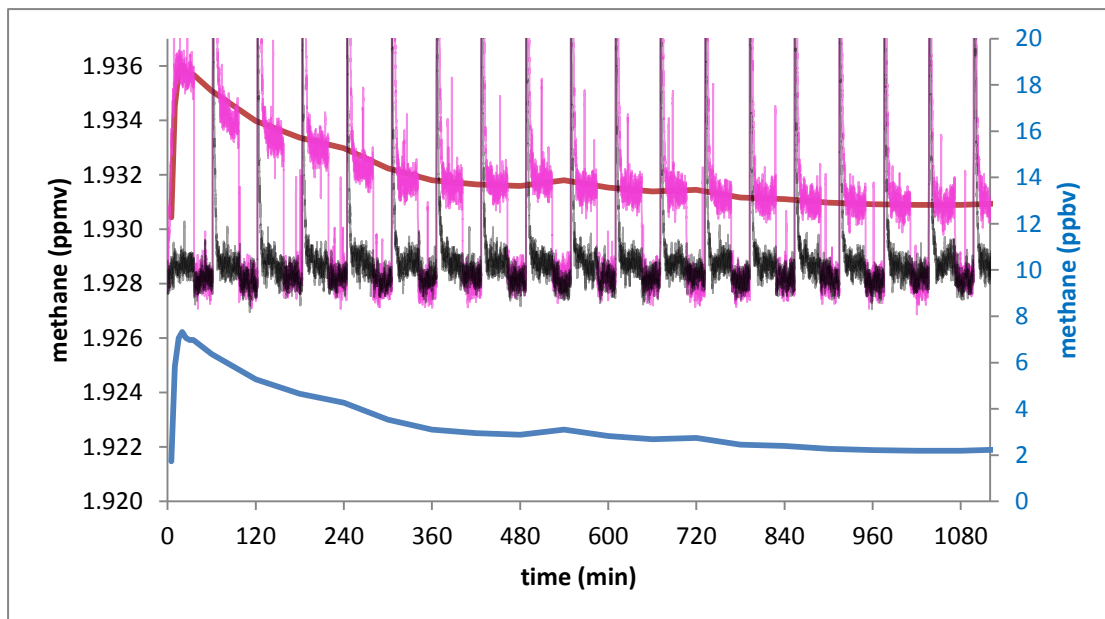


Figure 13: Methane mixing ratio of the first 19 hours of irradiation of experiment 2. The pink line denotes the time series of the raw measurements and the red line the hourly averaged values that are non-accumulation time. The black line shows the blank measurements (petri dish + gas + UV), while the blue line shows the hourly averaged meteoritic methane mixing ratio (red line – average blank value) which is shown on the secondary vertical axis (blue color).

After applying the above-mentioned data analysis, the recorded hourly averaged methane mixing ratio for experiments 1-4 was plotted in *Figure 14*.

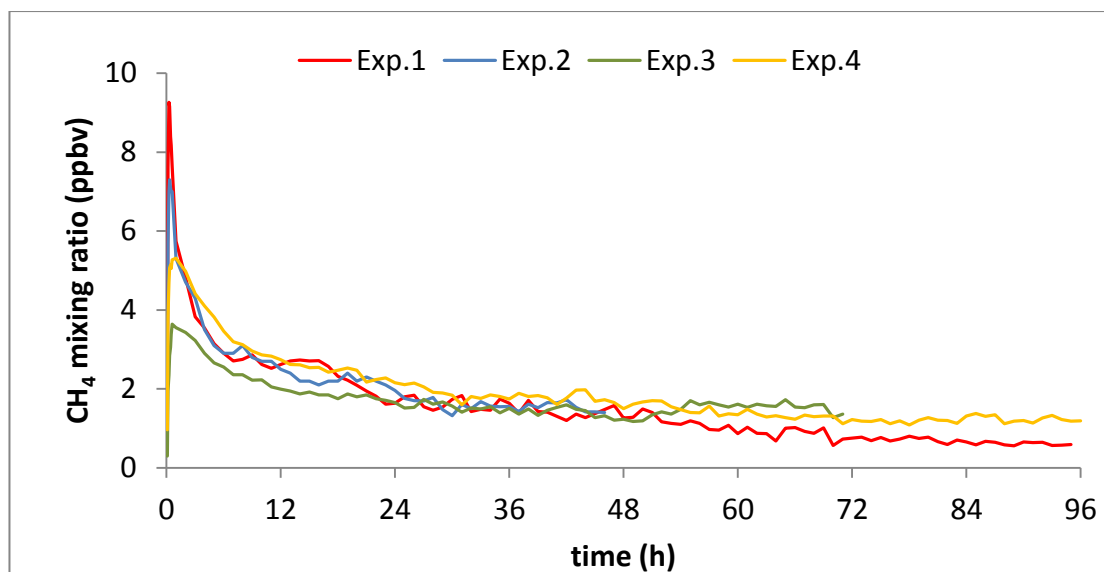


Figure 14: Hourly averaged produced meteoritic methane in parts per billion for experiment 1-4. The blank value (petri dish + gas + UV) was subtracted from the measurements. At t=0 the lamp was turned on.). The UV intensity exposure decreased by moving from experiment 1 to 4.

It was observed that in the first 30 minutes of irradiation, higher energy photons led to enhanced methane outgassing. At the beginning the methane mixing ratio of experiment 1 showed a peak at 9 ppbv, while the maximum value obtained in experiments 2, 3 and 4 reached 6.5, 3.5 and 5.2 parts per billion, respectively. The difference between experiments with respect to their methane production was minimized in a few hours. Initial peak values declined logarithmically in time ($R^2 > 0.87$) as it is shown in *Figure 15*. Experiments 1-3 accessed a value down to 1-2 ppbv in 24 hours, while experiment 4 needed four extra hours for its mixing ratio to go below 2 ppb. Experiment 1 that showed the highest methane emission in the first hour of UV exposure, acquired the lowest production level beyond 52 hours.

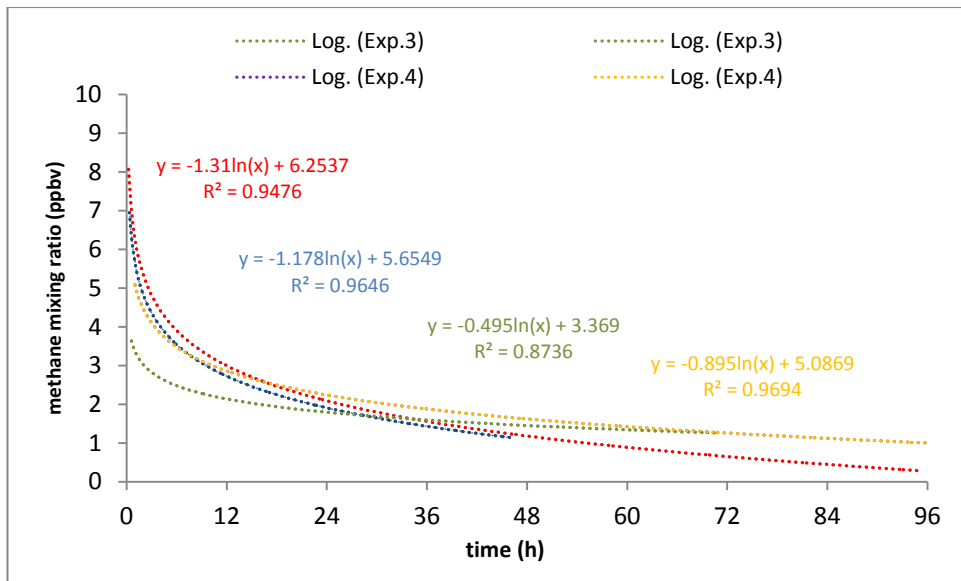


Figure 15: Logarithmic fit in methane mixing ratio of experiments 1 – 4. The equation of each fit as well as the corresponding R squared value is also displayed.

4.6.2 Emission rates

Figure 16 shows the emission rate of methane (in ng) for each experiment, as they were calculated from methane mixing ratio values and normalized per mass.

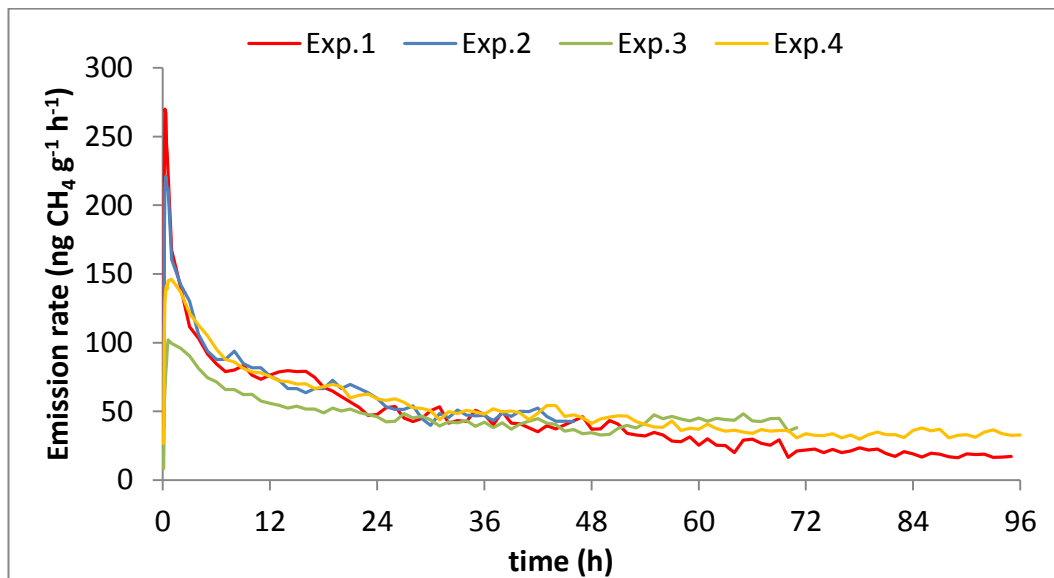


Figure 16: Emission rate of meteoritic methane in nanograms of produced methane per gram of dry weight per hour, for experiments 1-4. The emission rate value for each hour

was calculated according to the corresponding hourly averaged methane production (for which the blank was subtracted).

Since all meteorite samples had nearly the same weight, mass normalization didn't affect their relative distribution (as it is shown in *Figure 14*). Following the pattern of methane mixing ratio, emission rates showed a peak in the first 30 minutes. Experiment 3 and 4 reached a value of 102 and 141 ng CH₄ g⁻¹ h⁻¹. The logarithmic relation between the ultraviolet intensity and the emission rate in the first 30 minutes until a peak is reached is plotted in *Figure 17*.

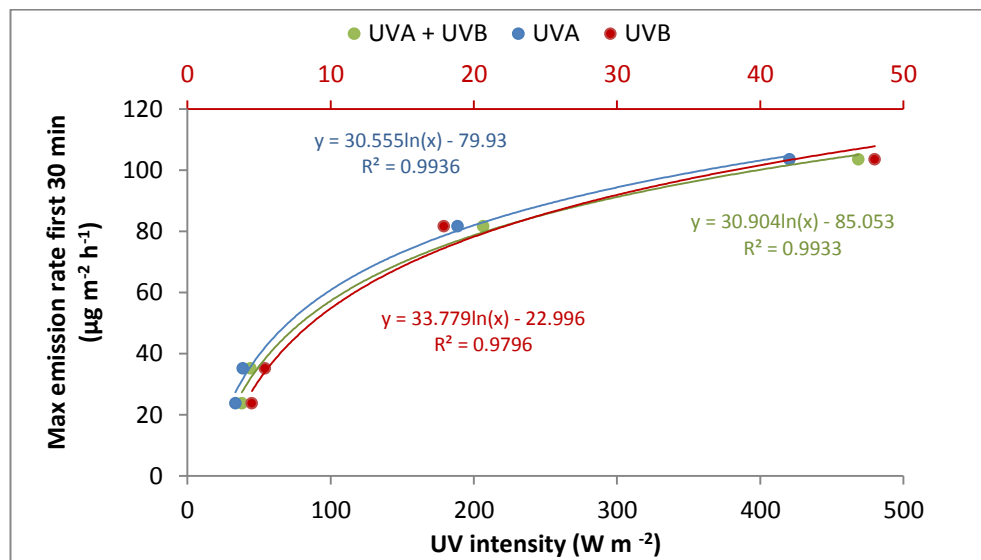


Figure 17: Maximum rate of methane emission on the first half hour of irradiation, under different UV intensities. The green line shows the total UV, while blue and red line show the corresponding UVA and UVB components respectively.

Similar experiments carried out by *Kepler et al., 2012* were characterized by similar UV intensities as experiments 3 and 4, only the sample meteorite mass was double ($\approx 200\text{mg}$). The observed emission rates in the first 25 minutes of irradiation ($1680\text{ng CH}_4 \text{ g}^{-1} \text{ hr}^{-1}$) were around 16 times higher than experiment 3 and 11 times larger than experiment 4.

Figure 16 reveals another significant difference between higher and lower level UV radiation experiments. Experiments 1 and 2 reached a high emission rate in the first

20 minutes of irradiation, at 269 and 221 ng CH₄ g⁻¹ hr⁻¹, which decreased to 50% in 2 and 4 hours respectively. On the other hand, the highest emission rate of experiment 3 / 4 (lower level UV) decreased to half only when 20 / 15 hours of irradiation were completed. After 24 hours all four experiments had similar emission rate values (46 – 63 ng CH₄ g⁻¹ h⁻¹). As mentioned for methane production, highest UV experiment 1 showed the lowest emission rate beyond 51 hours of irradiation.

Though experiment 4 was irradiated with a lower UVA/UVB intensity than experiment 3, it displayed higher emissions due to its increased surface of exposure. To further check the importance of the surface area of a sample rather than its mass, after the completion of 96 hours of irradiation of experiment 1 (with final methane mixing ratio reached at 1 ppbv), meteoritic grains were redistributed and re-irradiated for 24 hours more. *Figure 19* illustrates the results for which methane mixing ratio corresponding to redistributed material (dotted line) followed almost the same pattern (a bit lower after 5 hours) as the first UV exposure day of non-irradiated grains.

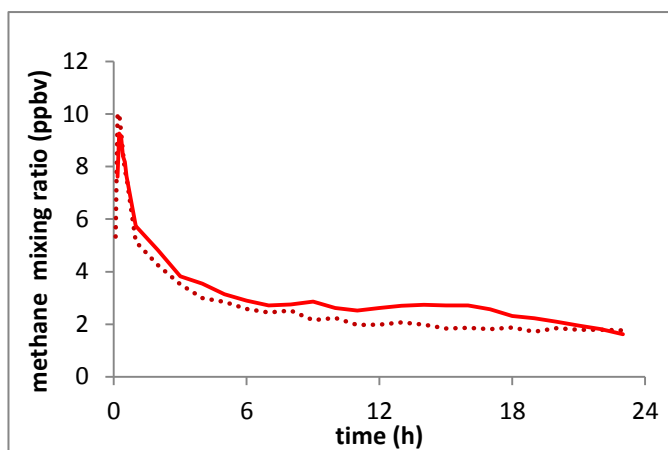


Figure 19: Mixing ratio of methane for 24 hours of irradiation at the beginning of experiment 1 (red line) and after redistributing the sample (dotted line) - after 96 hours of irradiation).

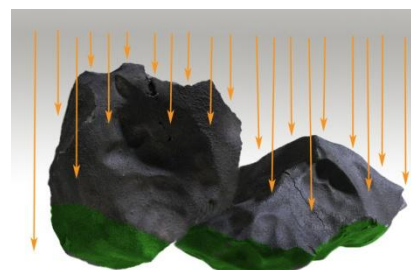


Figure 18: example of exposed (grey) /non exposed (green) areas of meteoritic grains

The result shows that a large fraction of the sample is not exposed to radiation (as shown in *Figure 18*); this can be either the bottom part of each grain, as well as material that is not on the top surface of the irradiated sample (covered by other

grains). This fact denoted the importance of the exposed meteoritic area in methane release and for this reason the emission rates were also chosen to be normalized per area (instead of per mass).

Figure 20 shows the hourly averaged emission rates of methane after they were normalized per exposed meteoritic surface (in $\mu\text{g m}^{-2}$).

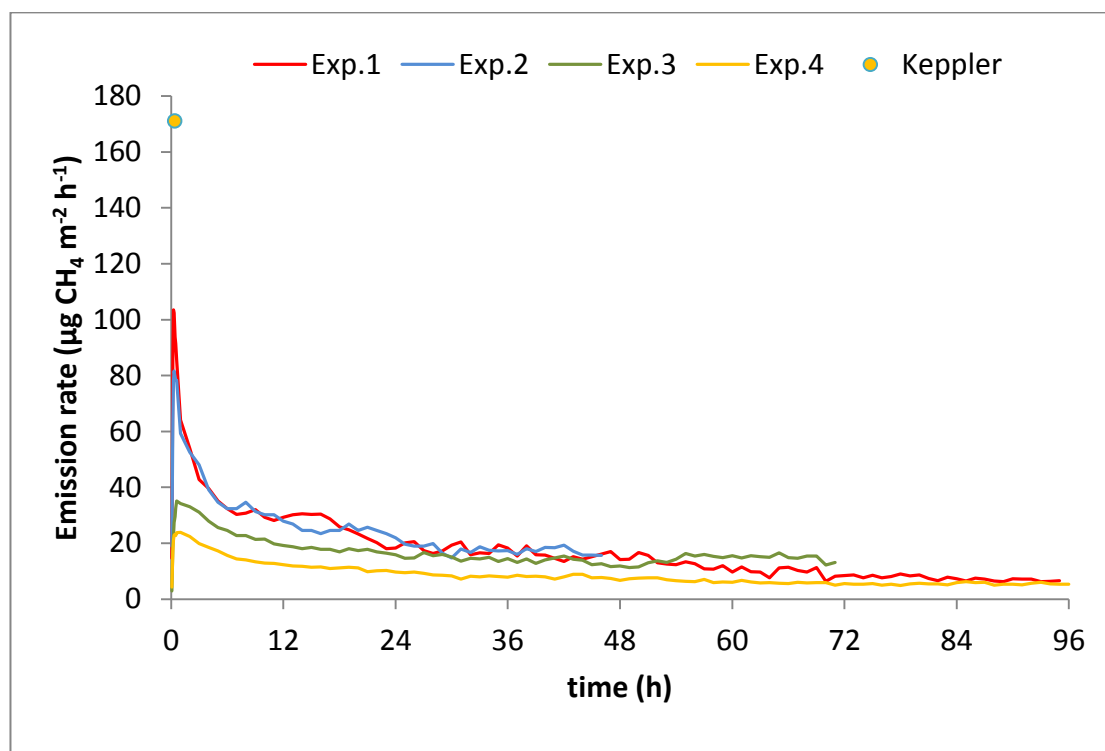


Figure 20: Emission rate of meteoritic methane in micrograms of produced methane per area (m^{-2}) per hour, for experiments 1-4. The emission rate value for each hour was calculated from the corresponding hourly averaged methane mixing ratio (from which the blank was subtracted). The yellow dot shows the maximum observed emission rate mentioned by *Kepler et al., 2012* for a double mass of sample and similar UV intensities as experiment 3 and 4.

In this case, the maximum emission rate of experiment 3 / 4 is only 5 / 8 times lower than the one mentioned by *Kepler, 2012*. Since the area covered by the sample is taken into account, the emission rate of experiments 3 and 4 are distributed in *Figure 20* according to their UV level of exposure (unlike *Figure 16* for which the larger surface of experiment 4 affected the emission rate). The initial range in emission rates

between 21 – 103 $\mu\text{g CH}_4 \text{ m}^{-2} \text{ h}^{-1}$ is reduced to 10 – 22 $\mu\text{g CH}_4 \text{ m}^{-2} \text{ h}^{-1}$ in 24 hours. Throughout the experimental period, methane from sample 4 is emitted at the lowest rates (lowest UV intensity experiment). In *Table 8*, a comparison is shown between the emission rates normalized by mass and by surface area.

Table 8: Difference between emission rate peaks during the first 30 minutes of irradiation of experiment 1-4 and time period needed for those values to drop to 50 %, when normalized per weight and per area. The parenthesis in experiments 3 and 4 denote how many times lower is the emission rate in comparison with the *Kepler, 2012* values.

Experiment	Per gram		Per area	
	Maximum Emission rate ($\text{ng CH}_4 \text{ g}^{-1} \text{ h}^{-1}$)	Time for max emission rate to go down to 50% (h)	Maximum Emission rate ($\mu\text{g CH}_4 \text{ m}^{-2} \text{ h}^{-1}$)	Time for max emission rate to go down to 50% (h)
1	269	2	103	2
2	221	4	78	4
3	105 (16↓)	20	32 (5↓)	24
4	141 (11↓)	16	21(8↓)	20
Kepler	1680		171	

4.6.3 Methane mass production

Figure 21 shows the total integrated production of CH_4 per gram of meteorite material over the course of the experiments. It can be seen that after one day of irradiation, all four experiments measured similar produced methane mass (1.50 - 2.09 $\mu\text{g g}^{-1}$) similar to the value from *Kepler et al., 2012* falls (1.65 $\mu\text{g g}^{-1}$). During the second day of UV interactions at least 1 μg of CH_4 was produced in each experiment. On the third day of irradiation 0.7 μg , 0.96 μg and 0.92 μg of methane were emitted from experiment 1, 3 and 4, respectively. The total mass production of methane at the end of experiment 1 reached at 4.25 $\mu\text{g g}^{-1}$ (96 hours irradiation), experiment 2 at 3.15 $\mu\text{g g}^{-1}$ (48 hours irradiation), 3.45 $\mu\text{g g}^{-1}$ (72 hours) for experiment 3 and 4.96 $\mu\text{g g}^{-1}$ (96 hours) for experiment 4.

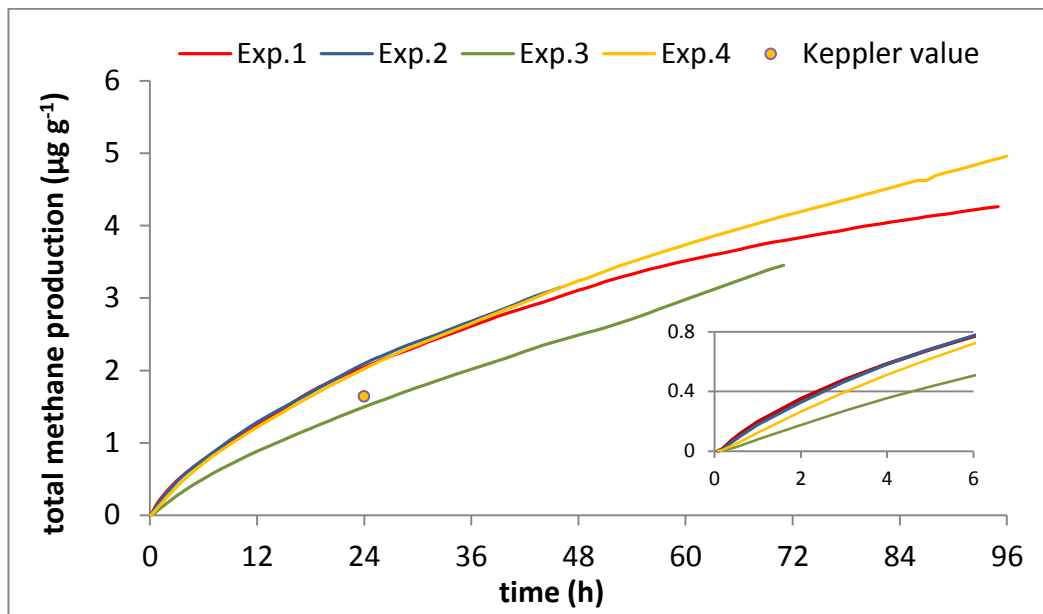


Figure 21: Total methane production in $\mu\text{g per gram}$ in micrograms per gram versus irradiation to time for experiments 1-4. The value calculated by *Kepler et al., 2012* after 24 hours of irradiation can be seen as a yellow dot. The plot on the bottom-left zooms on the produced methane in the first 6 hours of irradiation.

Figure 22 shows that when normalization is done per surface area, the cumulative methane production increases with increasing intensity, but only up to a certain intensity level at which the emission rate is apparently saturated.

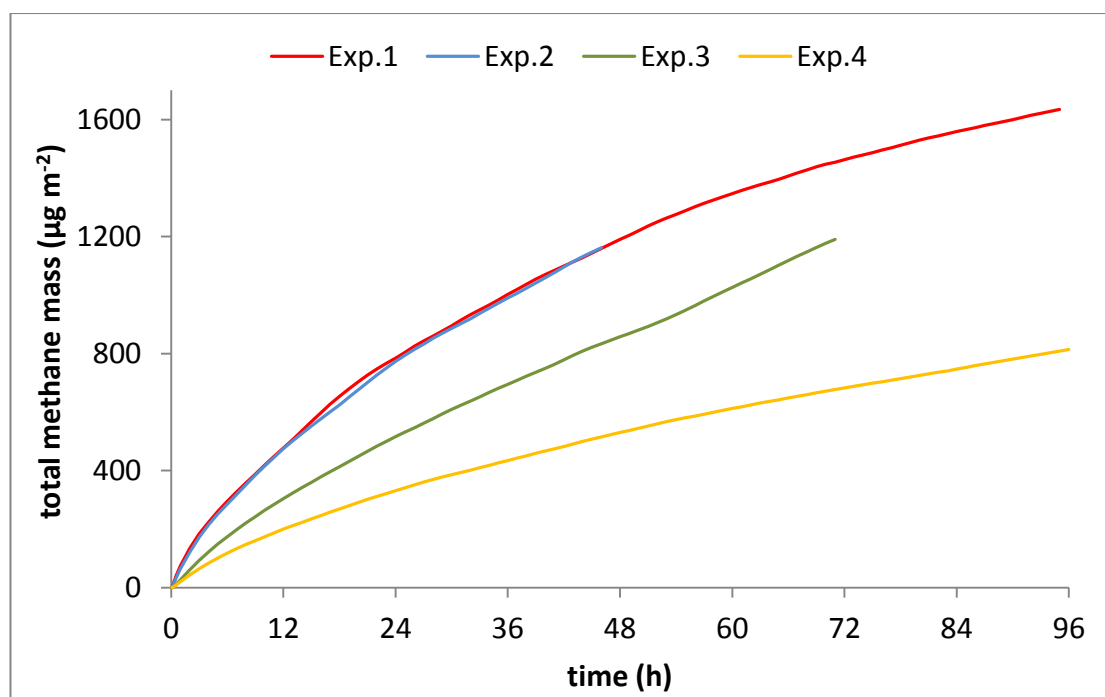


Figure 22: Total mass of produced methane in micrograms per area ($\mu\text{g m}^{-2}$) of sample in respect to time for experiments 1-4.

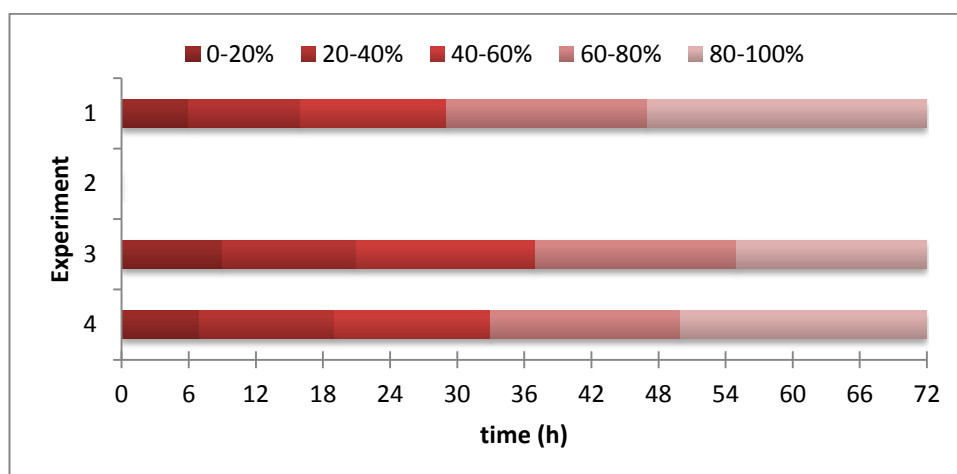
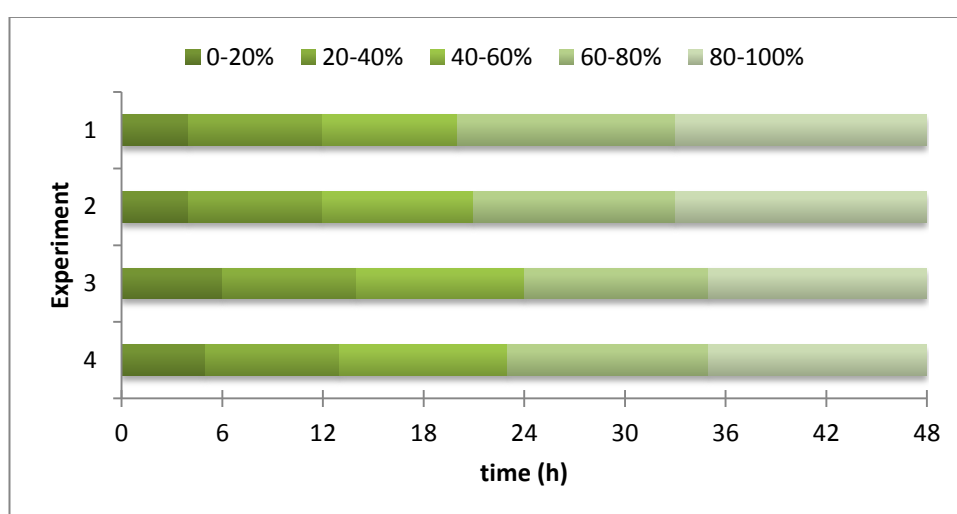
Table 9 compares the UVB intensity of experiments (from experiment 1 irradiation values), with the corresponding decrease in methane mass production. Despite the 63% reduction in UVB intensity during experiment 2, total methane mass production declined only by 2% after 48 hours of irradiation. UVB radiation was decreased during experiment 3 by 89% (relative to experiment 1), which was accompanied by a restriction in methane release by 34% in 24 hours. A tiny decrease of experiment 3 UVB intensity from 5.4 to 4.5 W m^{-2} (0.9 W m^{-2}) reduced total produced methane mass further by 36% (from experiment 3 value).

Table 9: Total methane production ($\mu\text{g m}^{-2}$) of experiments 1-4 after irradiation time of 24 hours and 48 hours. The numbers in each parenthesis denote the proportional decrease of each value with respect to the corresponding experiment 1 value.

	Experiment			
	1	2	3	4
UVB (W m^{-2})	48.0	17.9 (63%)	5.4 (89%)	4.5 (91%)
Total CH ₄ 24 h	785	773 (1%)	516 (34%)	332 (58%)

production in $\mu\text{g m}^{-2}$	48 h	1190	1173 (2%)	858 (28%)	530 (55%)
	72 h	1455	-	1190 (18%)	682 (53%)
	96 h	1634	-	-	814 (50%)

The proportional relationship among different intensity experiments and their UV induced methane production in time is shown in Figure 23a–c . Each color box represents a 20% fraction of the total methane production ($\mu\text{g m}^{-2}$) in 48 hours (Figure 23a), 72 hours (Figure 23b) and 96 hours (Figure 23c).



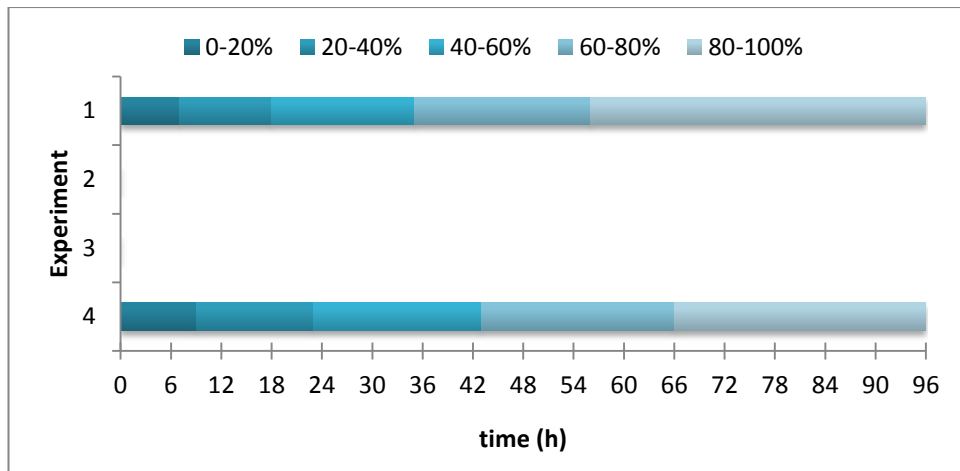


Figure 23: The different color boxes of each bar shows the 20% fractions of total methane release (in $\mu\text{g m}^{-2}$) after a. 48 hours (green), b. 72 hours (red) and c. 96 hours (red). From experiment 1 to 4, UV intensity decreases.

Despite the 28 – 55% (*Table 9*) difference in the 48 hour methane mass emission between higher and lower irradiation experiments, their temporal evolution was almost the same. As shown in *Figure 17a*, 20% of the total methane was produced in 4-6 hours, 40% between 12 – 15 hours, 60% and 80% among 19 – 24 hours and 33 – 35 hours, respectively. According to this pattern, the irradiation time of the targets was chosen.

4.6.3 Penetration depth estimation (from methane gas values)

Figure 24 shows the estimated penetration depth from the emission rate values of methane, according to the formulas denoted in section 3.3.5 and by assuming that all carbon is removed from each nanometer layer before UV photons can penetrate deeper.

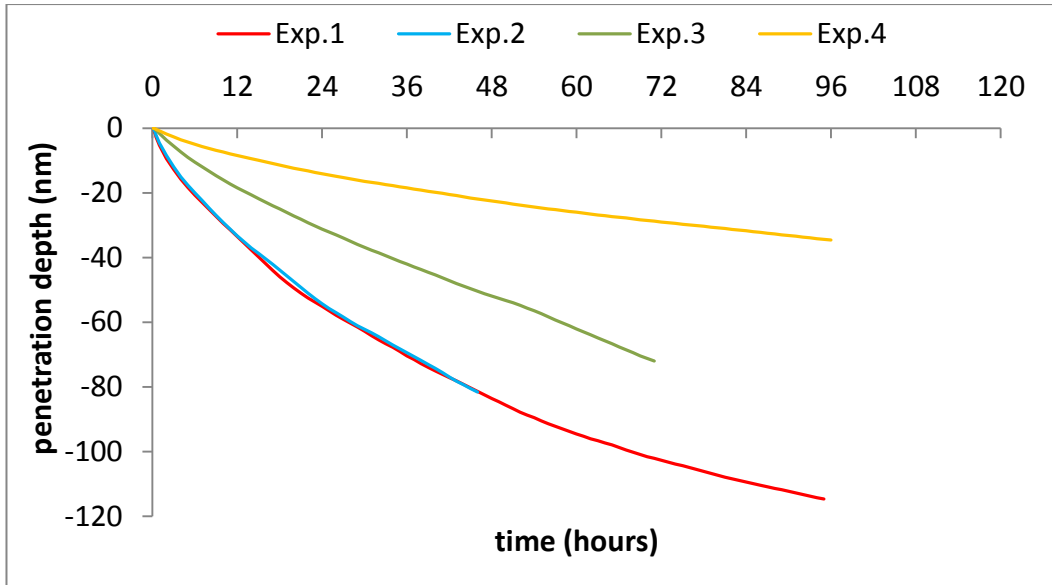


Figure 24: Penetration depth of UV photons as was estimated from emitted methane mass per area of each experiment under irradiation according to the calculation in section 3.3.5.

During high intensity experiments, ultraviolet photons reach bigger depths in the same time intervals (despite the 63% decrease from experiment 1 to 2). The gradient of UV penetration depth declines gradually in time, which can also be seen in *Figure 25* as a decrease in the penetration rate. After 96 hours it looks like radiation reached 110 nm below the top surface of the meteorite. The 90% drop in irradiation intensity during experiment 3 (in comparison to experiment 1) induced a reduction in the achievable depth by 63% (-52 nm) in 48 hours. A drop in irradiance by less than 1 W m⁻² (from experiment 3 to 4) restrained the reachable depth by further 40% (-22 nm) in 48 hours. After 96 hours of irradiation, experiment 4 photons did not reach a depth below -40 nm. This is also reflected in the low rates recorded in *Figure 25*.

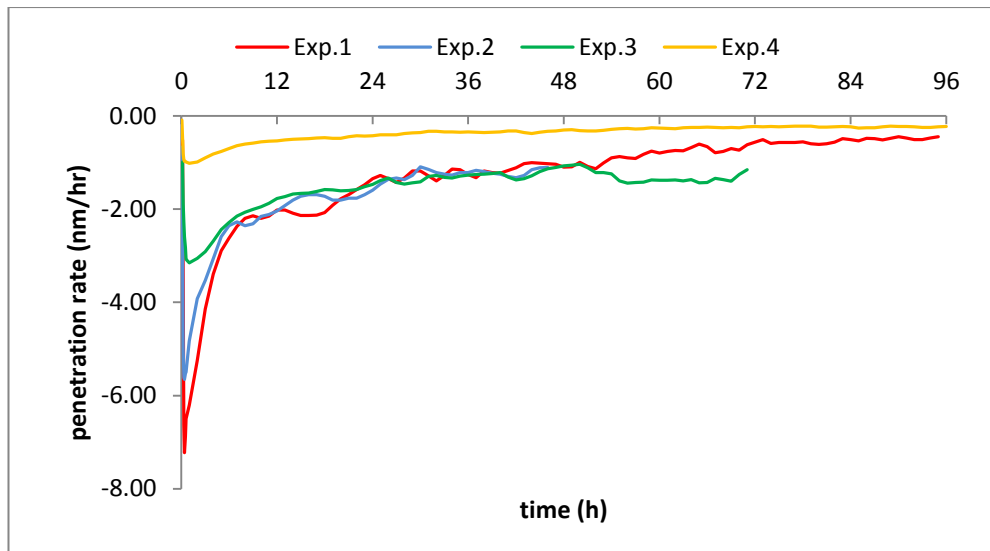


Figure 25: Rate at which different intensities of ultraviolet radiation penetrate the surface of the meteorite. It was estimated according to the outgassing methane per area values of each experiment.

4.7 Irradiated target experiments

For the purposes of this project only the blank and the longest/strongest irradiated target, H72h, results are presented.

4.7.1 Surface topography

The topography image of the blank target is shown in *Figure 27* (Scanning electron image or SEI image), which is zoomed by 40 times. The bubbles at the lower left side of the image represent holes in the top surface of the resin. The selected area for nanoSIMS application is denoted in a grey box and its 900 times zoomed image is illustrated in *Figure 26* (SEI image).

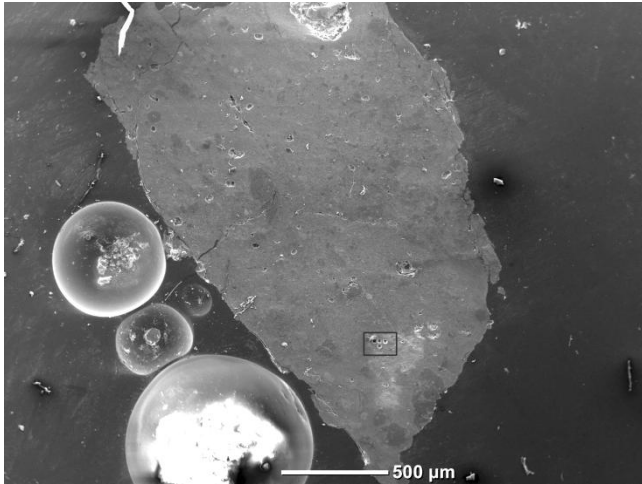


Figure 27: SEI image of the blank target zoomed by 40 times. The grey box shows the spot where nanoSIMS was applied.

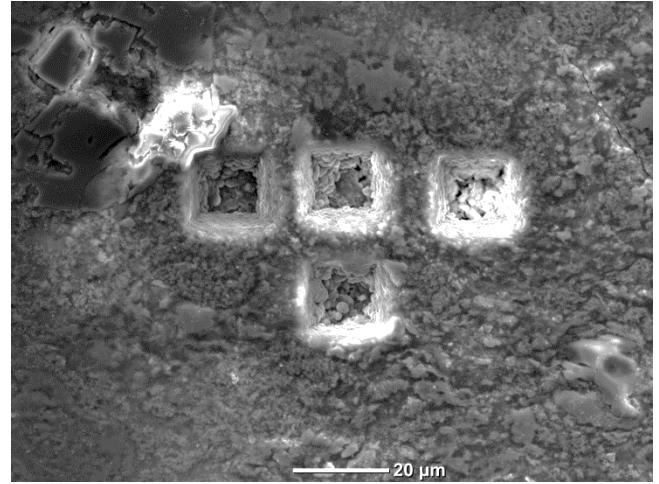


Figure 26: The 900 times zoomed crater area denoted as a grey box in *Figure 20*. The length scale can be seen at the bottom of each image.

The depth expansion of the 15 x 15 μm craters created on the surface of the meteorite can be clearly seen which demonstrates the destructive ability of the nanoSIMS. It looks like the depth of nanoSIMS analysis surpassed a few micrometers which exceed significantly the desired depth scale of just a few hundreds of nanometers. As it was mentioned in section 3.3.3, the depth analysis of the UU nanoSIMS is not known yet.

Figure 28 shows the BEI image (Backscattered Electron Image) of the crater area, where the more bright areas denote the presence of elements with larger atomic numbers.

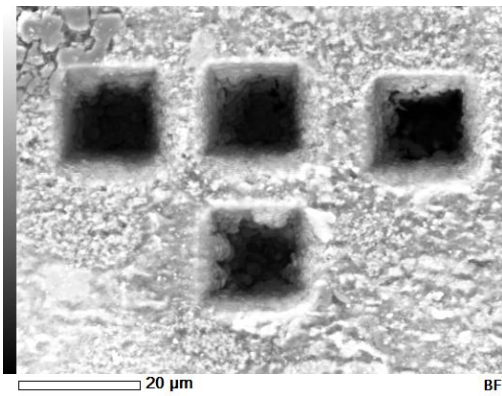


Figure 28: BEI image of the four craters of the blank target. Brighter areas denote the presence of elements with larger atomic number. The black colour of the craters does not imply that there are no heavy atoms there, but that the SEM cannot measure inside the craters.

The resulting SEM image of backscattered electrons is shown in *Figure 29* (BEI image). A comparison with the elemental maps of *Figure 26* reveals that the lighter grey areas dominating the target consist of iron oxides, while the darker grey spots shown in the black and grey box are silicate minerals (Si and O). *Figure 30* shows the SEM zooming area 1 (black box). The location of craters 1 to 6 is visible. Again according to the elemental maps (their area is shown as a grey box in *Figure 29*), nanoSIMS analysis corresponding to craters 5 and 6 was applied in iron oxide rich spots; minerals which are considered to catalyze organic reactions with UV and the release of methane.

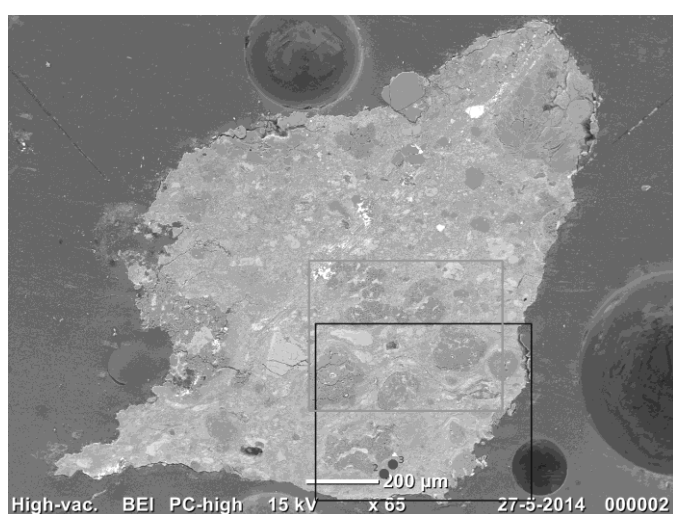


Figure 29: BEI image of target H72 (x 65). Less bright spots in the scale of grey denote elemental areas with lower atomic numbers. NanoSIMS applied area is shown by a black box (*Figure 26*). The grey box shows the area of the elemental map of *Figure 26*.

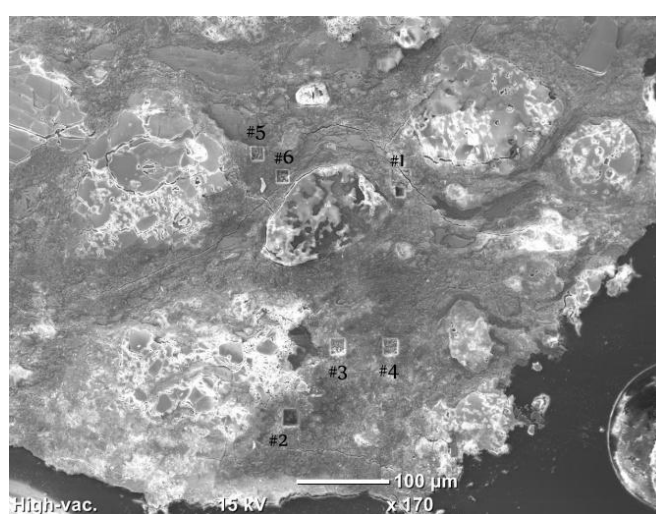


Figure 30: SEI image of nanoSIMS applied area of target H72h, where the location of craters 1 to 6 can be seen.

Individual elemental maps of each target were made for to carbon, iron, silicon, oxygen, magnesium, sulfur and calcium. To better visualize different minerals, groups consisting of three elements were created and their elemental maps were combined into one image. The first category included iron, sulfur and oxygen (to reveal iron oxides), the second one was made of magnesium, silicon and oxygen (to locate silicate crystals), while the third group was made of carbon, calcium and aluminum (to see their spatial distribution relation with the other two categories).

Figure illustrates the BEI image and the combined elemental maps of the grey box area of Figure 29.

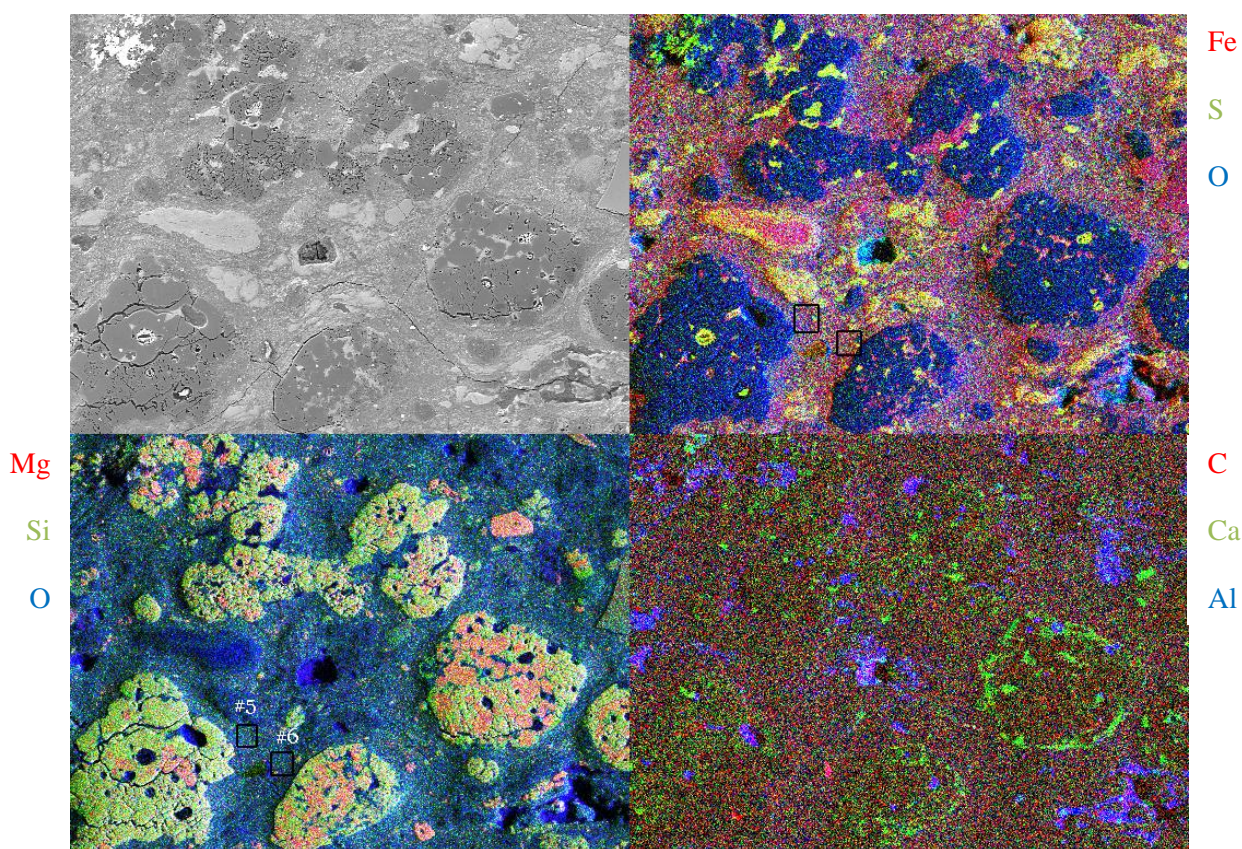


Figure 31: The top-left shows the BEI image of the grey box of Figure , while the other images show the elemental maps from the SEM analysis. Top-right map: red = Fe, green = S, blue = O; bottom-left map: red = Mg, green = Mg, blue = O; bottom-right map: red = C, green = Ca, blue = Al. Craters 5 and 6 of the H72h target are indicated by two black boxes on the bottom-left and top-right map.

The darker grey areas of the BEI image are enriched in silicon, oxygen and magnesium which might correspond to phyllosilicate crystals that are associated with catalyzation of organic material formation. The lighter grey areas surrounding these crystals show a high signal in iron and oxygen that denotes the presence of iron oxides. No carbon grains were detected (grains made mostly by carbon). For the bright red areas (bottom-right map) surface topography imaging indicated that they represent surface contamination areas (dust or bacterial colonies) and they were avoided for the nanoSIMS application. On the contrary carbon is shown to be dispersed all around the matrix of the target.

The depth profile of ^{13}C and ^{12}C of target H72 (colored lines) as well as the carbon values of the blank (grey dotted lines) are shown in *Figure 2*.

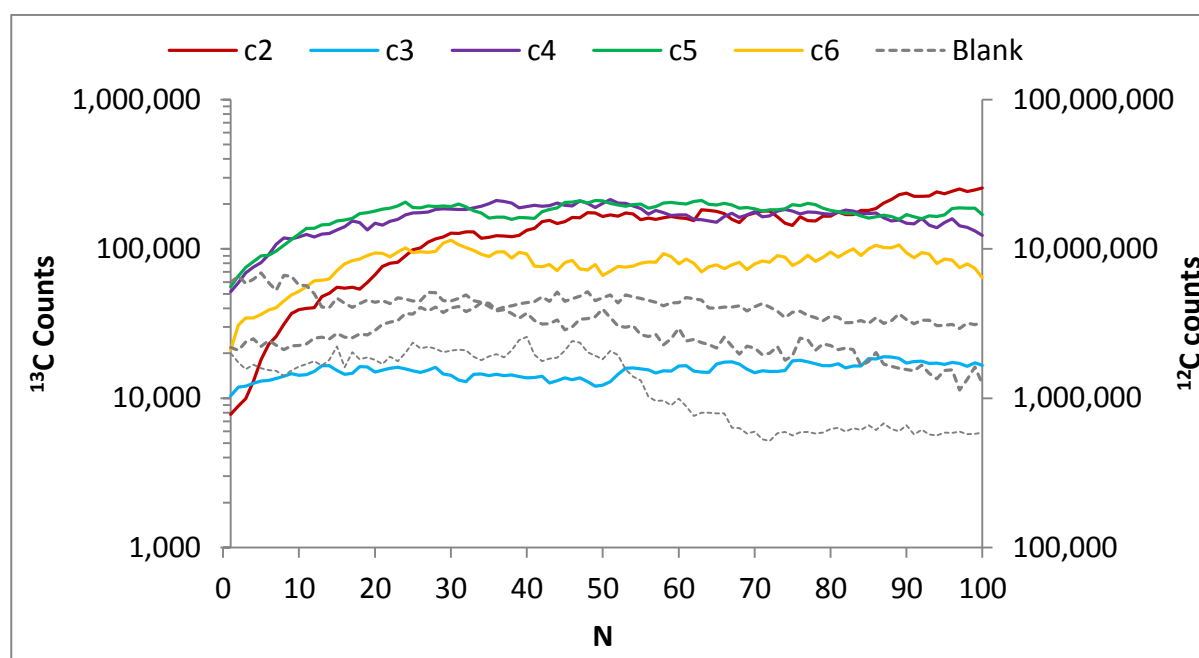


Figure 32: Coloured lines show the ^{13}C and ^{12}C depth profile corresponding to craters 2 – 6 (c2 to c6) of the H72h target. The grey dotted lines show the blank values per scanned layer (N) that was measured from 3 craters of the blank target.

^{13}C counts for target H72h varied approximately between 8×10^3 and 2×10^5 and for the blank among $2 - 5 \times 10^4$. The corresponding ^{12}C counts followed the same pattern but were two orders of magnitude higher (10^5 to 10^7 for H72 and $2 - 5 \times 10^6$ for the blank).

To spot a depth profile that would describe the UV induced carbon loss of the first top layers of the meteorite, initial carbon counts of a crater were expected to be lower and increase gradually per scanned layer. They should reach a maximum value and remain relatively stable, at the point of the maximum achievable penetration depth of ultraviolet photons.

By looking at the crater image (*Figure 21*), it looks like the vertical distance between the top surface and the bottom of the hole is in the scale of a few crystals (can be

seen from the 'wall of each crater) which means nanoSIMS might have reached a depth of a few micrometers. Since the first scanned layers (N) are believed to be in the range of a few hundred nanometers, they will be the only ones taken into account and described further on (up to N = 30).

In general, the carbon in target H72h seems to be depleted near the surface, as expected if it had been removed by the surface treatment. Around the 30th scanned layer they reached a maximum number carbon counts. On the contrary, the blank values showed no depleted depth profile. Their ¹³C and ¹²C values remained approximately constant from the top layer down to the 30th layer. Only the data from crater 2 and 3 showed initial carbon counts that were lower than the blank indications. Crater 2 initial carbon count reached the blank value at the scanning of the sixth layer (N = 6) by the nanoSIMS, to reach 1.3×10^6 from 7×10^5 . Despite the lower than blank carbon counts of crater 3, its carbon content remained stable during the nanoSIMS analysis. The total count rates of the remaining craters were higher than the blank, even for the surface layers.

The penetration depth of UV light can also be seen when ¹³C / ¹²C rates is taken into account. UV irradiation has been shown to volatilize light ¹²C preferentially (Keppler et al, 2012), so the C remaining near the surface should be enriched in ¹³C. The ¹³C / ¹²C ratio should decrease with depth and after some point (where no more UV interactions occurred and thus that's the maximum penetration depth) maintain a relatively stable value.

Figure 33 a – e shows the isotopic carbon ratio of craters 2 – 6 of the H72h target. An enrichment in the heavy isotope ¹³C is shown for the first layers of c2 and c6. The remaining craters didn't reveal any fractionation pattern for the top layers. The increase in carbon counts after the third layer of c2, increases the Poisson error and thus the accuracy of the measurement.

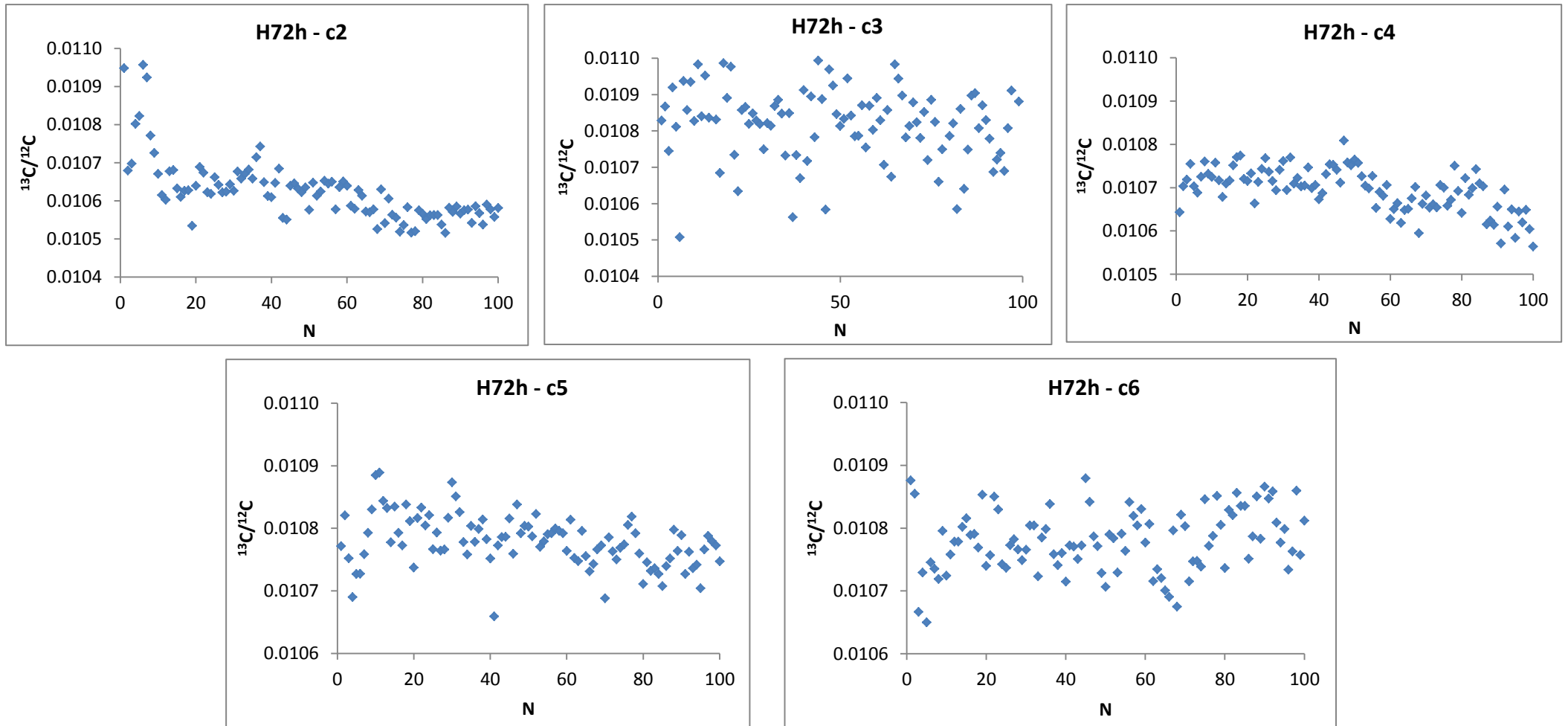


Figure 293 a – e: $^{13}\text{C}/^{12}\text{C}$ ratio of crater 2 – 6 of the target H72h for the first 100 layers scanned by the nanoSIMS.

During nanoSIMS application, also the depth profiles of iron (^{56}Fe), silicon (^{28}Si), oxygen (^{18}O) and magnesium (^{24}Mg) were measured. Fe with Mg and Si with ^{18}O counts have shown a high correlation up to 0.99. *Figure 34* and *35* show the depth profiles of different elements for craters of target H72h and the blank.

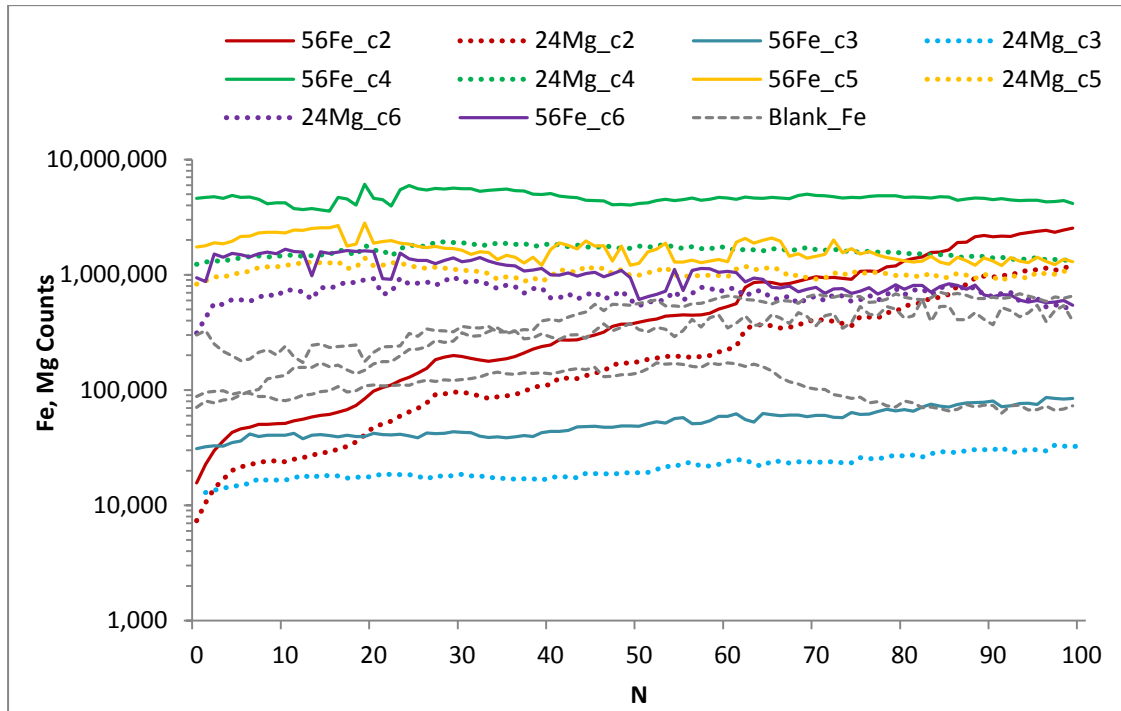


Figure 304: Iron and magnesium depth profile of target H72h is shown by continued and dotted lines, respectively. The grey dashed lines denote the iron values recorded for each layer for the three craters of the blank target. No measurements were taking concerning the Mg values of the blank.

Beyond c2 and c3, all remaining craters showed higher Fe counts than the corresponding blank counts. This shows that that the targets of the blank have less Fe, so it may be a different kind of mineral. Both magnesium and iron counts of crater 2 and 3 were 1 – 2 times of magnitude lower than c4 – c6, whose values were around 10^6 counts per scanned layer. C The iron measurements of crater 2 and crater 6 were the only two that noted a decrease in Fe and Mg counts of the first scanned layers. The rate of change in elemental counts remained approximately stable for all the craters.

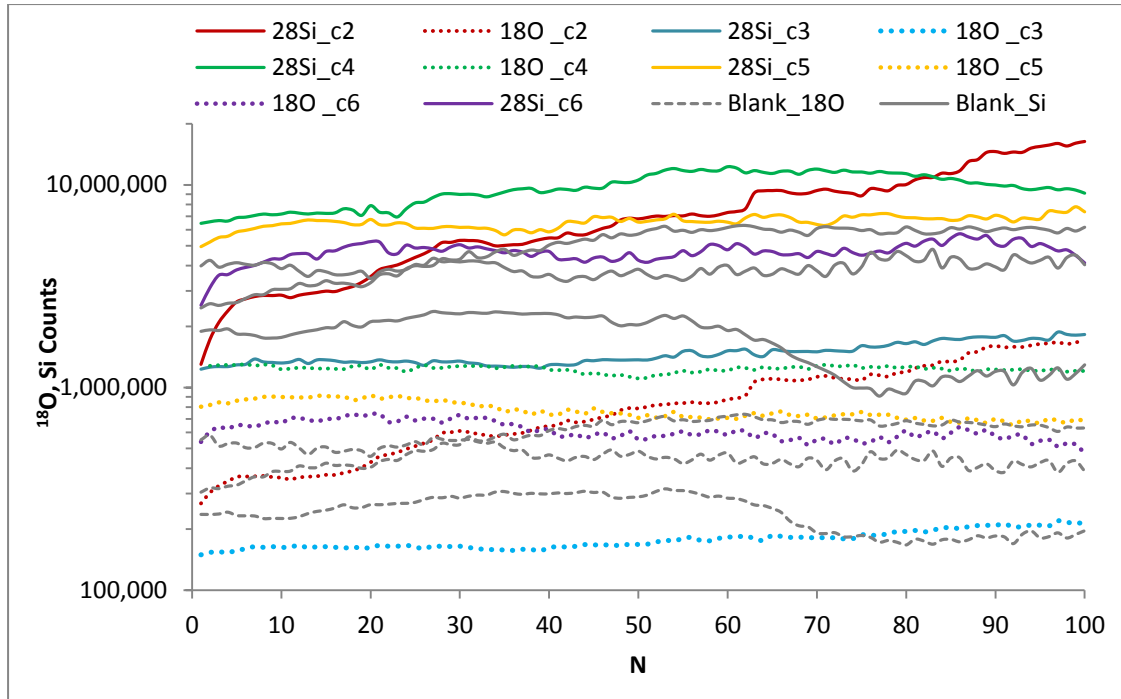


Figure 35: Si and ¹⁸O depth profiles of target H72h are shown by continued and dotted lines, respectively. Grey lines denote Si values for the blank craters, while dashed grey lines represent ¹⁸O values.

¹⁸O counts were around 10 times smaller than Si counts but they both varied by one order of magnitude (¹⁸O between 10⁵-10⁶ and Si 10⁶-10⁷). All crater values were relatively close to the blank range counts. c2 and c6 were the only craters with a drop in their initial silicon and heavy oxygen counts (no initial ¹⁸O count drop for c6).

Table 10: The abundance range of each element is shown for craters c2 to c6 and the blank for all the scanned areas over layer 20.

Count range	1 ≤ N ≤ 20			
	10 ⁴ – 10 ⁵	10 ⁵ - 10 ⁶	10 ⁶ – 10 ⁷	10 ⁷ – 10 ⁸
c2	¹³ C, Fe, Mg	¹⁸ O	¹² C, Si	
c3	¹³ C, Fe, Mg	¹⁸ O	¹² C, Si	
c4		¹³ C, ¹⁸ O	Fe, Si, Mg	¹² C
c5		¹³ C, ¹⁸ O	Fe, Si, Mg	¹² C
c6	¹³ C	¹⁸ O, Mg	¹² C, Si, Fe	
Blank	¹³ C	¹⁸ O, Fe	¹² C, Si	

^{18}O and Si have shown the same scale of counts for all craters and the blank. The close elemental relation between c2, c3, c6 with the blank can be seen in respect to elements ^{13}C , ^{12}C , ^{18}O and Si. Crater 2 and 3 are depleted in Fe and Mg in comparison with c6 (and the blank for Fe). On the other hand c4 and c5 vary significantly from the remaining craters and blank. They were located in Fe and Mg enriched spots and they show 10 times higher ^{13}C and ^{12}C all the rest cases.

To further check for depletion near the surface, the ratios of carbon versus the remaining elements were calculated. Since the counts of lighter carbon were two scales of magnitude larger than heavy carbon, the use of ^{12}C measurements was used to decrease the Poisson error and thus improve the accuracy of the results.

In general, the ratios acquired a stable value after the scanning of the 20th layer which was considered as the depth beyond which no UV interactions occurred. To better visualize the results, each ratio of the first 30 layers was normalized with the average ratio between $N = 20$ and $N = 30$.

Figure 36 a – d shows the normalized ratios of ^{12}C with the rest of the elements that were measured by the nanoSIMS, between the surface and the 30th layer. Continuous-colored lines show the evolution of the ratios of craters c2 to c6 as the nanoSIMS was penetrating deeper under the meteorite surface of target H72, while grey-dotted represent the three craters of the blank target. Values smaller than 1 denotes depletion of ^{12}C or enrichment of the counterpart element. If the normalized ratio shows a value larger than 1, then enrichment in ^{12}C or depletion of the other element can be concluded.

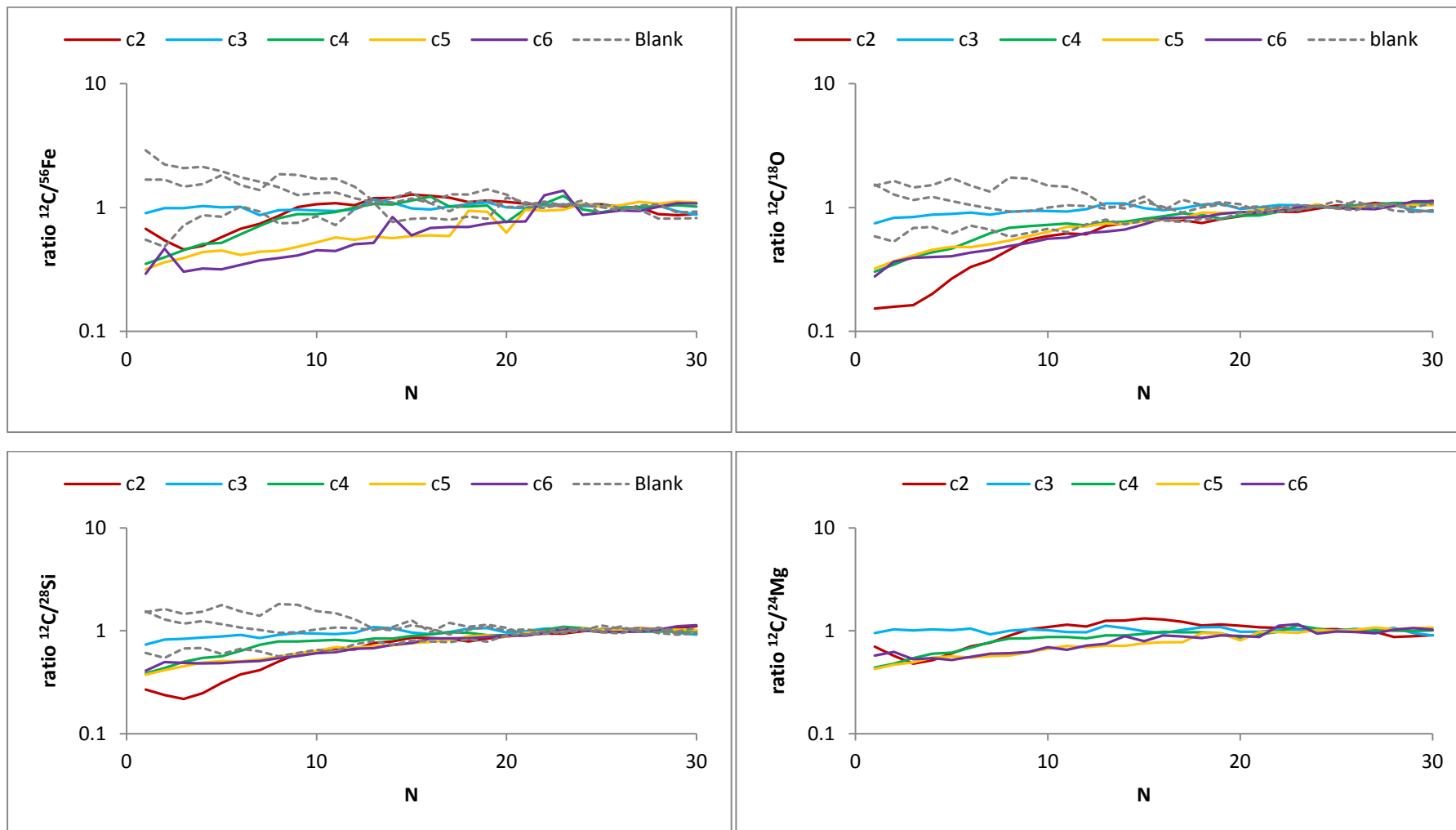


Figure 36 a-d: Elemental ratio target H72h of light carbon, ^{12}C , to a. ^{54}Fe , b. ^{18}O , c. ^{28}Si and d. ^{24}Mg , normalized with ratio of UV non-affected deeper layers (N=20 to 30). Dotted-grey lines show the ratio of the blank target. No blank measurements were taken for ^{24}Mg .

Crater 3 of target H72h showed no significant alterations in the isotopic ratios, even close to the surface. On the other hand, the remaining craters of target H72h have shown a drop in the normalized ratio value from the surface down to layer 15 – 20. c5 and c6 acquired almost identical ratio values for all layers. The ratios of $^{12}\text{C}/^{24}\text{Mg}$ showed the less deviation from value 1, while $^{12}\text{C}/^{18}\text{O}$ obtained the most. Concerning the non-UV affected blank craters, two of them showed ratio values slightly higher than 1. The third blank crater revealed a depth ratio pattern similar to craters c2 and c4 – c6 of H72h, though on a smaller scale.

5 Conclusions – Discussion

5.1 Methane emission

Irradiation experiments have proven that CH₄ is a direct product of UV interactions with meteorites that are classified as carbonaceous chondrites. UV photons cause the initiation of photochemical reactions of organics on and below the surface of the meteorite eventually leading to their degradation with simultaneous outgassing of volatile hydrocarbons.

The validity and accuracy of recorded methane signals was confirmed with various tests. The standard deviation of the data during the instrument stability checks (section 4.1) confirmed the stability and accuracy of the Picarro analyser at ± 1 ppb. Long term gas stability tests in combination with background gas control checks before/after/during (valve switch to mode 2) experiments have revealed the high precision of the analyser. They have also excluded any possibility that background gas perturbations could have interacted with the measured methane values sourcing from the meteorite. In addition, long term blank tests have shown a constant blank signal, that didn't exceed 1.1 ppbv even beyond 96 hours of UV exposure.

5.2 Emission rates of methane

Despite the large UV intensity differences of the four methane emission experiments (experiment 1 – 4), they have all shown a methane signal peak in the first 35 minutes of irradiation. Maximum emission rates declined in 24 hours, yet maintained notable values by the time each experiment was terminated. This is in contrast to the extrapolation by Keppler (Keppler et al., 2012) where they expected that emissions would basically stop after 12 hours of irradiation. Observed smaller scale fluctuations (*Figure 16, Figure 20*) of the emission rates were probably due to the diverse mineral composition and the non-uniform distribution of the organic material inside the meteorite. Higher emission signals that reported before (Keppler

et al., 2012) are probably due to the high mineral heterogeneity that is observed in Murchison meteorite.

When meteorite grains were redistributed, the emission signal increased from 1 – 2 ppbv to reach a peak at approximately 10 ppbv that gradually declined. This proved that a large fraction of the meteorite sample was not exposed to photons. It also denoted the importance of mechanical mixing on Mars in the release of methane. Martian winds expose fresh meteorite material to UV radiation by shaking them or breaking them down to smaller grains. Long term irradiation experiments should be made in the future that will also include mechanical mixing, to record total potential methane production per gram of meteoritic material. In case no mechanical mixing is taken in mind, emission rates should be normalized per exposed surface area and not per mass.

5.3 Methane emission in carbon limited / photon limited conditions

Despite the fact that UV intensity of experiment 2 was 63% lower than experiment 1, their methane emission ranged at approximately similar levels. It can be said that the photodegradation of organics in both cases was happening at the same rates and was determined only by the availability of carbon. On the other hand, a restriction in UV flux by 89% (from experiment 1) in experiment 3 caused the drastic drop of emission values; a fall which was doubled on reducing experiment's 4 UV intensity value (from experiment 3) by 16%. The intensity of UV photons was the limiting factor for experiments 3 and 4. Since Schuerger et al. 2012 proved that each latitude of the surface of Mars is carbon limited (section 1.4.5.6), it is concluded that experiments 1 and 2 are representative for Martian conditions in respect to UV – induced methane production. A UV intensity value between experiment 2 and 3 is the boundary between carbon – limited and photon – limited conditions, and this needs to be determined in the future. Martian radiation levels seem to be close to this boundary. It also needs to be investigated if methane mass production in photon limited environments, given sufficient time, will reach carbon limited total values. The analysis of the rest of the targets from the second part of experiments will also help in a better interpretation of methane emission results.

5.4 Penetration depth from methane mass values

Experiments 1 – 4 were accomplished under pressure conditions of 1000 mbar. Methane mass production augments by 2 to 3 times when used pressures are down to Martian values (5 – 10 mbar) (reference). Estimated penetration depth of carbon – limited conditions (experiment 1 and 2) in section 1.4.5.4, is expected to go from -120 nm (after 96 hours of irradiation) down to a value between -240 and -360 nm. The accuracy of this method in estimating the penetration depth will be evaluated after the penetration depth will be determined from the nanoSIMS analysis.

5.5 Lack of carbon grains

SEM analysis has revealed the lack of organic grains (that consist almost entirely of carbon) inside the meteorite. On the contrary, the presence of carbon was found to be diffused all around the matrix of the meteorite targets. It could be hypothesized that this area of the meteorite had undergone intense aqueous alteration reactions that dispersed carbon grains (section 1.4.4.3). On the other hand, the lack of cracks filled with organic material denotes that in situ aqueous alteration should have been limited.

5.6 Carbon depletion

NanoSIMS analysis has shown a carbon-depleted depth profile for most of the studied craters of target H72h, yet not for the blank craters. It appears that approximately the first 20 – 25 scanned layers interacted with ultraviolet radiation, which caused the photodegradation of molecules containing carbon with its subsequent removal from the meteorite matrix as volatile gases. The last depth for which carbon depletion is observed can be considered as the maximum penetration depth of UV photons. The gradual increase of ^{13}C and ^{12}C counts from the surface to the deeper layers shows that carbon removal efficiency of UV photons decreases with depth. Scanned surfaces beyond the depleted layers (beyond $N \approx 25$) that show

relatively stable carbon counts represent non – UV affected layers. These areas show the carbon pattern of the surface layers prior to UV exposure.

The carbon levels of craters 2, 4 and 5 showed similar values (for layers beyond the penetration depth of UV). Despite the fact that crater 4 and 5 followed an almost identical depletion path, crater 2 was characterized by one order of magnitude of greater surface carbon depletion; a trend that was also followed in the rest of the chemically active layers. Probably the high presence of Mg in craters 4 and 5 (2 orders of magnitude larger than crater 2) reduced the reactivity of carbon molecules. Since magnesium silicate minerals are weak absorbers of UV wavelengths (section 1.4.5.2), surface reactions that release radicals and induce degradation of molecules were restricted. The organics in magnesium rich areas shown by the elemental maps of SEM analysis are not expected to show a strong carbon – depleted depth profile if nanoSIMS is applied over them. It also looks like the presence of magnesium and iron is related by an enhanced level in carbon elements, according to c4 and c5 carbon counts. This reveals the importance of the mineral composition of the meteorite in the reactivity of its organics with UV light. The range of carbon counts between different craters of each non – UV affected scanned layers proves the previously reported high heterogeneity of elements in carbonaceous chondrites (Le Guillou et al., 2014).

$^{13}\text{C} / ^{12}\text{C}$ ratios have shown ^{13}C enrichment only for the first layers of crater 2 of target H72h. Such an enrichment was expected due to its preferential volatilization of ^{12}C by the UV.

Further analysis of the remaining targets is needed for the complete understanding of carbon depletion in time and under different UV intensities.

5.7 Penetration depth of UV radiation

The big question that remains is the depth of each layer ablated by the nanosims (distance between N values), which will also enlighten the understanding and accurate interpretation of the isotopic measurements. This can be accomplished by the use of an atomic force microscope which will allow the quantification of the depth of each crater. Since the number of scanned surfaces is known for each crater (total N), the vertical scale of each layer can be calculated.

By knowing the penetration depth of UV, the conversion rate of meteoritic carbon to methane on Mars per day can be calculated. The knowledge of this will allow future rovers be sensitive enough to detect daily carbon fluxes.

5.8 Carbon vs other elements

The ratios of C versus other elements was used to check for depletion at the surface. Carbon was removed by UV while others (Fe, Mg, O, Si), did not since they are not volatile. By assuming these elements are distributed smoothly, they may be used as a «calibration» for instrument sensitivity variations with depth. The initial, abrupt drop that is observed in the first few layers of some elements is due to the implantation of cesium ions at the beginning of nanoSIMS application to increase the signal.

6 Appendix

6.1 Carboxylic acids

Low molecular weight ($C < 10$) monocarboxylic acids were the most abundant dissolvable group of compounds that were extracted from the Murchison meteorite, with a concentration of approximately 332 ppm. Acetic acid has shown the highest concentration of all the monocarboxylic acids; up to $770.1 \text{ nmol g}^{-1}$. These molecules extend up to chains of C_{10} with more than 50 different species reported to date (Huang et al., 2005). They appear either as straight chains or as more complex-branched molecules. Their structural profusion is confined as the number of the carbon chain increases in length (Gilmour, 2003)^{vii}. The occurrence of branches at every possible point of the long chain reveals a genetic environment where gas phase reactions led to a rich in free radicals and ions surrounding. Such reactions are exothermic, thus they have very low activation energies and can occur at extremely low temperatures (10-100K); a fact that unveils the extraterrestrial provenance of these monocarboxylic acids (Huang et al., 2005).

Forty dicarboxylic acids up to chains of nine carbons were also identified in Murchison, as well as α -hydroxycarboxylic acids. The existence of the latter one (along with α -amino acids) shows that they were synthesized through Strecker chemical reactions^{viii} and reveals that the meteorite did not undergo temperatures that would induce their pyrolytic disintegration (Gilmour, 2003).

6.2 Amino acids

The composition of different parts of the Murchison meteorite varied with respect to amino acids; some due to contamination from Earth's environment or different extraction techniques. The average Murchison amino acid chemical formula is $C_4H_9NO_2$ (Pizzarello et al., 1991), with glycine as the simplest spotted molecule. The number of amino acids

^{vii} On grounds of reaction kinetics, carbon isotopic fractionation is minimized as the carbon chain expands in length. Lighter charged molecules (i.e. ions or radicals with ^{12}C) react more rapidly with molecules rather than heavier ones such as ^{13}C , leading to the enrichment of monocarboxylic acids with ^{12}C (you did not really explain that).

^{viii} Strecker synthesis: the aqueous part of the Miller-Urey experiment where chemical reactions between simple inorganic molecules (i.e. CH_2O , HCN and NH_3) lead to the formation of organic molecules

extracted^{ix} from the matrix exceeds one hundred (α -, β -, γ -, δ -, ϵ - amino acids) among which eight have identical counterparts in proteins^x found in Earth's biosphere^{xi} (Pizzarello and Shock, 2010). The existence of all these substances reveals the possibility and range at which extraterrestrial abiotic chemistry can synthesize organic molecules similar to biomolecules. However, the heterogeneity of Murchison components conflicts the selectivity found in biochemistry, creating questions if such meteorite material could have contributed to the primordial soup^{xii}, leading to evolutionary biochemical paths.

Isotopic analyses have revealed that amino acids were enriched in D, ¹³C and ¹⁵N compared to terrestrial material, with values up to +40‰ ($\delta^{13}\text{C}$) and +2500‰ (δD) (Pizzarello et al., 1991). High deuterium values are most likely a result of low temperature amino synthesis through Strecker reactions during aqueous alteration in an interstellar cloud^{xiii} ^{xiv} (Pizzarello

^{ix} amino acid fractions are isolated by paper chromatography

^x Glycine, alanine, proline, valine, leucine, isoleucine, aspartic acid and glutamic acid

^{xi} All the proteins found in living organisms of Earth (by present) are build up by only 20 amino acids

^{xii} A solution rich in organic molecules in the primordial oceans in which life is considered to have been created

^{xiii} The theory behind amino acid formation in carbonaceous chondrites describes a frozen parent body abundant in volatiles (especially water and deuterium). At some point this body is subjected to warming which initiates a period of aqueous phase chemistry and thus amino acid formation (it can be maintained internally for some period even if the surface is frozen). Eventually, volatile substances are lost and nonvolatile organic material, such as amino acids, is reserved (Pizzarello et al., 1991).

^{xiv} The theory behind amino acid formation in carbonaceous chondrites describes a frozen parent body abundant in volatiles (especially water and deuterium). At some point this body is subjected to warming which initiates a period of aqueous phase chemistry and thus amino acid formation (it can be maintained internally for some period even if the surface is frozen). Eventually, volatile substances are lost and nonvolatile organic material, such as amino acids, is reserved (Pizzarello et al., 1991).

et al., 1991). Some Murchison chiral amino acids which are not present in organisms have been proven to possess the same elemental configuration as proteins of living cells.

6.3 Hydrocarbons

A fraction of the Murchison meteorite is made of hydrocarbon molecules. Aliphatic hydrocarbons with chains below 10 carbons are dominated by benzene and alkyl-benzene, while for longer structures n-alkanes prevail. The majority of identified aromatic hydrocarbons were constituted of fluoranthene, pyrene and PAHs (polycyclic aromatic hydrocarbons (Gilmour, 2003).

6.5 Experimental pictures



Figure 317: Experimental setup: normal air is flushed from the cylinder to the reactor inside the chamber, through the mass flow controllers. It leaves the reactor and ends up at the Picarro analyser.

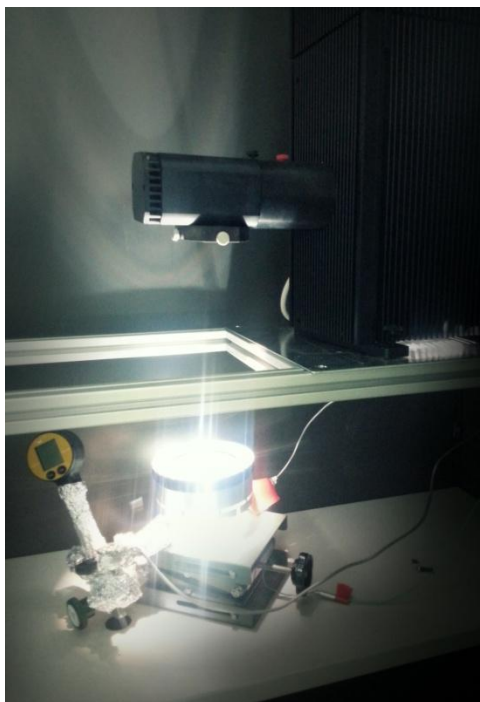


Figure 328: Reactor under irradiation from the Xenon light source



Figure 339 a-c: Reactor view from different angles.

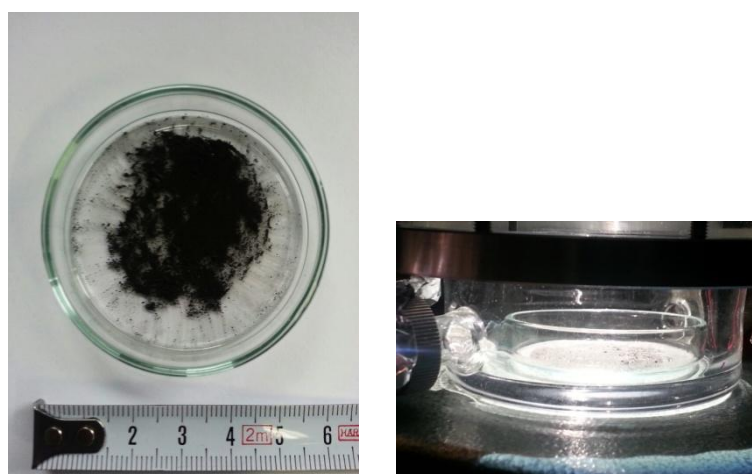


Figure 40 a – b: Petri dish with meteoritic material under irradiation (right) and meteoritic material surface area (experiment 4) inside the petri dish (left)

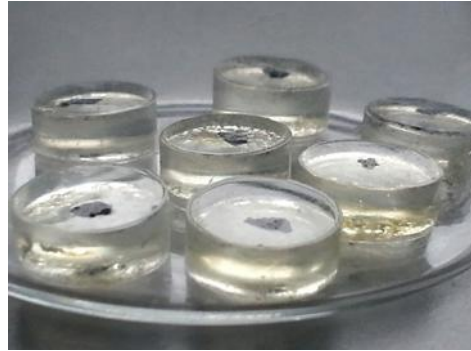


Figure 41 a – b: Targets with meteorite fractions sized around 1-2mm, to be analyzed by a NanoSIMS.

- Airieu, S. a., Farquhar, J., Thiemens, M.H., Leshin, L. a., Bao, H., Young, E., 2005. Planetesimal sulfate and aqueous alteration in CM and CI carbonaceous chondrites. *Geochim. Cosmochim. Acta* 69, 4167–4172. doi:10.1016/j.gca.2005.01.029
- Alexander, C.M.O., Newsome, S.D., Fogel, M.L., Nittler, L.R., Busemann, H., Cody, G.D., 2010. Deuterium enrichments in chondritic macromolecular material—Implications for the origin and evolution of organics, water and asteroids. *Geochim. Cosmochim. Acta* 74, 4417–4437. doi:10.1016/j.gca.2010.05.005
- Atreya, S.K., Mahaffy, P.R., Wong, A.-S., 2007. Methane and related trace species on Mars: Origin, loss, implications for life, and habitability. *Planet. Space Sci.* 55, 358–369. doi:10.1016/j.pss.2006.02.005
- Bartoszek, M., Wecks, M., Jakobs, G., Möhlmann, D., 2011. Photochemically induced formation of Mars relevant oxygenates and methane from carbon dioxide and water. *Planet. Space Sci.* 59, 259–263. doi:10.1016/j.pss.2010.09.008
- Cockell, C., 2000. The Ultraviolet Environment of Mars: Biological Implications Past, Present, and Future. *Icarus* 146, 343–359. doi:10.1006/icar.2000.6393
- Etiopie, G., Oehler, D.Z., Allen, C.C., 2011. Methane emissions from Earth ' s degassing: a reference for Mars. *Planet. Sp. Sci.* 59, 182–195.
- Flynn, G.J., 1996. The delivery of organic matter from asteroids and comets to the early surface of Mars. *Earth Moon Planets* 72, 469–474.
- Flynn, J., 1990. An assessment of the meteoritic contribution to the Martian soil. *J. Geophys. Res* 95, 14497 – 14509.
- Formisano, V., Atreya, S., Encrenaz, T., Ignatiev, N., Giuranna, M., 2004. Detection of methane in the atmosphere of Mars. *Science* 306, 1758–61. doi:10.1126/science.1101732
- Gilmour, I., 2003. Structural and Isotopic Analysis of Organic Matter in Carbonaceous Chondrites, in: *Treatise in Geochemistry*. pp. 269–290.
- Huang, Y., Wang, Y., Alexandre, M.R., Lee, T., Rose-Petruck, C., Fuller, M., Pizzarello, S., 2005. Molecular and compound-specific isotopic characterization of monocarboxylic acids in carbonaceous meteorites. *Geochim. Cosmochim. Acta* 69, 1073–1084. doi:10.1016/j.gca.2004.07.030
- Keppler, F., Vigano, I., McLeod, A., Ott, U., Früchtl, M., Röckmann, T., 2012. Ultraviolet-radiation-induced methane emissions from meteorites and the Martian atmosphere. *Nature* 486, 93–6. doi:10.1038/nature11203
- Krasnopolsky, V. a., 2012. Search for methane and upper limits to ethane and SO₂ on Mars. *Icarus* 217, 144–152. doi:10.1016/j.icarus.2011.10.019

- Krasnopolsky, V.A., Maillard, J.P., Owen, T.C., 2004. Detection of methane in the martian atmosphere: evidence for life? *Icarus* 172, 537–547.
doi:10.1016/j.icarus.2004.07.004
- Krot, A.N., Keil, K., Scott, E.R.D., 2007. Classification of Meteorites, in: *Treatise in Geochemistry*. pp. 2–44.
- Le Guillou, C., Bernard, S., Brearley, A.J., Remusat, L., 2014. Evolution of organic matter in Orgueil, Murchison and Renazzo during parent body aqueous alteration: In situ investigations. *Geochim. Cosmochim. Acta* 131, 368–392.
doi:10.1016/j.gca.2013.11.020
- Lefevre, F., Forget, F., 2009. Observed variations of methane on Mars unexplained by known atmospheric chemistry and physics. *Nature* 460, 720–723.
doi:10.1016/j.pss.2010.08.021
- Lehmann, K.K., Berden, G., Engeln, R., 2009. An Introduction to Cavity Ring- Down Spectroscopy, in: *Cavity Ring-Down Spectroscopy: Techniques and Applications*. pp. 1–26.
- Miller, S.L., Urey, H.C., 1959. Organic compound synthesis of the primitive Earth. *Science* (80-.). 130, 245–51.
- Mumma, M.J., Villanueva, G.L., Novak, R.E., Hewagama, T., Bonev, B.P., Disanti, M.A., Mandell, A.M., Smith, M.D., 2009. Strong Release of Methane on Mars in Northern Summer 2003. *Science* (80-.). 323, 1041–1045.
- Navarro-González, R., Vargas, E., de la Rosa, J., Raga, A.C., McKay, C.P., 2010. Reanalysis of the Viking results suggests perchlorate and organics at midlatitudes on Mars. *J. Geophys. Res.* 115, E12010.
doi:10.1029/2010JE003599
- Patel, M.R., Zarnecki, J.C., Catling, D.C., 2002. Ultraviolet radiation on the surface of Mars and the Beagle 2 UV sensor. *Planet. Space Sci.* 50, 915–927.
doi:10.1016/S0032-0633(02)00067-3
- Pizzarello, S., Krishnamurthy, R. V, Epstein, S., Cronin, J.R., 1991. Isotopic analyses of amino acids from the Murchison meteorite. *Geochim. Cosmochim. Acta* 55, 905–10.
- Pizzarello, S., Shock, E., 2010. The organic composition of carbonaceous meteorites: the evolutionary story ahead of biochemistry. *Cold Spring Harb. Perspect. Biol.* 2, a002105. doi:10.1101/cshperspect.a002105
- Poch, O., Noblet, a., Stalport, F., Correia, J.J., Grand, N., Szopa, C., Coll, P., 2013. Chemical evolution of organic molecules under Mars-like UV radiation conditions simulated in the laboratory with the “Mars organic molecule irradiation and evolution” (MOMIE) setup. *Planet. Space Sci.* 85, 188–197.
doi:10.1016/j.pss.2013.06.013

- Schuerger, A.C., Clausen, C., Britt, D., 2011. Methane evolution from UV-irradiated spacecraft materials under simulated martian conditions: Implications for the Mars Science Laboratory (MSL) mission. *Icarus* 213, 393–403.
doi:10.1016/j.icarus.2011.02.017
- Schuerger, A.C., Moores, J.E., Clausen, C.A., Barlow, N.G., 2012. Methane from UV-irradiated Carbonaceous Chondrites under Simulated Martian Conditions. *J. Geophys. Res.* 117.
- Scott, E., Krot, A., 2014. Chondrites and Their Components, in: *Treatise in Geochemistry*. pp. 66–125.
- Shkrob, I. a, Chemerisov, S.D., Marin, T.W., 2010. Photocatalytic decomposition of carboxylated molecules on light-exposed martian regolith and its relation to methane production on Mars. *Astrobiology* 10, 425–36.
doi:10.1089/ast.2009.0433
- Vigano, I., Weelden, H. Van, Holzinger, R., Keppler, F., Mcleod, A., 2008. Effect of UV radiation and temperature on the emission of methane from plant biomass and structural components. *Biogeosciences* 5, 937–947.
- Webster, C.R., Mahaffy, P.R., Atreya, S.K., Flesch, G.J., Farley, K. a, 2013. Low upper limit to methane abundance on Mars. *Science* 342, 355–7.
doi:10.1126/science.1242902
- Wong, A.-S., 2003. Chemical markers of possible hot spots on Mars. *J. Geophys. Res.* 108, 5026. doi:10.1029/2002JE002003

7 References

- Airieau, S. a., Farquhar, J., Thiemens, M.H., Leshin, L. a., Bao, H., Young, E., 2005. Planetesimal sulfate and aqueous alteration in CM and CI carbonaceous chondrites. *Geochim. Cosmochim. Acta* 69, 4167–4172.
- Alexander, C.M.O., Newsome, S.D., Fogel, M.L., Nittler, L.R., Busemann, H., Cody, G.D., 2010. Deuterium enrichments in chondritic macromolecular material— Implications for the origin and evolution of organics, water and asteroids. *Geochim. Cosmochim. Acta* 74, 4417–4437.
- Atreya, S.K., Mahaffy, P.R., Wong, A.-S., 2007. Methane and related trace species on Mars: Origin, loss, implications for life, and habitability. *Planet. Space Sci.* 55, 358–369.
- Bartoszek, M., Wecks, M., Jakobs, G., Möhlmann, D., 2011. Photochemically induced formation of Mars relevant oxygenates and methane from carbon dioxide and water. *Planet. Space Sci.* 59, 259–263.
- Cockell, C., 2000. The Ultraviolet Environment of Mars: Biological Implications Past, Present, and Future. *Icarus* 146, 343–359.
- Etioppe, G., Oehler, D.Z., Allen, C.C., 2011. Methane emissions from Earth ' s degassing: a reference for Mars. *Planet. Sp. Sci.* 59, 182–195.
- Flynn, G.J., 1996. The delivery of organic matter from asteroids and comets to the early surface of Mars. *Earth Moon Planets* 72, 469–474.
- Flynn, J., 1990. An assessment of the meteoritic contribution to the Martian soil. *J. Geophys. Res* 95, 14497 – 14509.
- Formisano, V., Atreya, S., Encrenaz, T., Ignatiev, N., Giuranna, M., 2004. Detection of methane in the atmosphere of Mars. *Science* 306, 1758–61.

- Gilmour, I., 2003. Structural and Isotopic Analysis of Organic Matter in Carbonaceous Chondrites, in: *Treatise in Geochemistry*. pp. 269–290.
- Huang, Y., Wang, Y., Alexandre, M.R., Lee, T., Rose-Petrucci, C., Fuller, M., Pizzarello, S., 2005. Molecular and compound-specific isotopic characterization of monocarboxylic acids in carbonaceous meteorites. *Geochim. Cosmochim. Acta* 69, 1073–1084.
- Keppler, F., Vigano, I., McLeod, A., Ott, U., Früchtl, M., Röckmann, T., 2012. Ultraviolet-radiation-induced methane emissions from meteorites and the Martian atmosphere. *Nature* 486, 93–6.
- Krasnopolsky, V. a., 2012. Search for methane and upper limits to ethane and SO₂ on Mars. *Icarus* 217, 144–152.
- Krasnopolsky, V.A., Maillard, J.P., Owen, T.C., 2004. Detection of methane in the martian atmosphere: evidence for life? *Icarus* 172, 537–547.
- Krot, A.N., Keil, K., Scott, E.R.D., 2007. Classification of Meteorites, in: *Treatise in Geochemistry*. pp. 2–44.
- Le Guillou, C., Bernard, S., Brearley, A.J., Remusat, L., 2014. Evolution of organic matter in Orgueil, Murchison and Renazzo during parent body aqueous alteration: In situ investigations. *Geochim. Cosmochim. Acta* 131, 368–392.
- Lefevre, F., Forget, F., 2009. Observed variations of methane on Mars unexplained by known atmospheric chemistry and physics. *Nature* 460, 720–723.
- Lehmann, K.K., Berden, G., Engeln, R., 2009. An Introduction to Cavity Ring-Down Spectroscopy, in: *Cavity Ring-Down Spectroscopy: Techniques and Applications*. pp. 1–26.
- Miller, S.L., Urey, H.C., 1959. Organic compound synthesis of the primitive Earth. *Science* (80-). 130, 245–51.

- Mumma, M.J., Villanueva, G.L., Novak, R.E., Hewagama, T., Bonev, B.P., Disanti, M.A., Mandell, A.M., Smith, M.D., 2009. Strong Release of Methane on Mars in Northern Summer 2003. *Science* (80-.). 323, 1041–1045.
- Navarro-González, R., Vargas, E., de la Rosa, J., Raga, A.C., McKay, C.P., 2010. Reanalysis of the Viking results suggests perchlorate and organics at midlatitudes on Mars. *J. Geophys. Res.* 115, E12010.
- Patel, M.R., Zarnecki, J.C., Catling, D.C., 2002. Ultraviolet radiation on the surface of Mars and the Beagle 2 UV sensor. *Planet. Space Sci.* 50, 915–927.
- Pizzarello, S., Krishnamurthy, R. V, Epstein, S., Cronin, J.R., 1991. Isotopic analyses of amino acids from the Murchison meteorite. *Geochim. Cosmochim. Acta* 55, 905–10.
- Pizzarello, S., Shock, E., 2010. The organic composition of carbonaceous meteorites: the evolutionary story ahead of biochemistry. *Cold Spring Harb. Perspect. Biol.* 2, a002105.
- Poch, O., Noblet, a., Stalport, F., Correia, J.J., Grand, N., Szopa, C., Coll, P., 2013. Chemical evolution of organic molecules under Mars-like UV radiation conditions simulated in the laboratory with the “Mars organic molecule irradiation and evolution” (MOMIE) setup. *Planet. Space Sci.* 85, 188–197.
- Schuerger, A.C., Clausen, C., Britt, D., 2011. Methane evolution from UV-irradiated spacecraft materials under simulated martian conditions: Implications for the Mars Science Laboratory (MSL) mission. *Icarus* 213, 393–403.
- Schuerger, A.C., Moores, J.E., Clausen, C.A., Barlow, N.G., 2012. Methane from UV-irradiated Carbonaceous Chondrites under Simulated Martian Conditions. *J. Geophys. Res.* 117.
- Scott, E., Krot, A., 2014. Chondrites and Their Components, in: *Treatise in Geochemistry*. pp. 66–125.

- Shkrob, I. a, Chemerisov, S.D., Marin, T.W., 2010. Photocatalytic decomposition of carboxylated molecules on light-exposed martian regolith and its relation to methane production on Mars. *Astrobiology* 10, 425–36.
- Vigano, I., Weelden, H. Van, Holzinger, R., Keppler, F., Mcleod, A., 2008. Effect of UV radiation and temperature on the emission of methane from plant biomass and structural components. *Biogeosciences* 5, 937–947.
- Webster, C.R., Mahaffy, P.R., Atreya, S.K., Flesch, G.J., Farley, K. a, 2013. Low upper limit to methane abundance on Mars. *Science* 342, 355–7.
- Wong, A.-S., 2003. Chemical markers of possible hot spots on Mars. *J. Geophys. Res.* 108, 5026.
- Yongsong H., W. Y. (2005). Molecular and compound-specific isotopic characterization of monocarboxylic acids in carbonaceous meteorites. *Geochimica et Cosmochimica Acta* (Vol. 69, pp. 1073-1084).